Collective Expansion in High-Energy Heavy-Ion Collisions at CERN SPS Energies

- single particle distributions and two particle interferometry -

ShinIchi Esumi

to be submitted to the Department of Physics for a Doctor of Science Degree at the Hiroshima University

4th of July, 1995

Abstract

Single particle distributions and two particle interferometry are measured in the NA44 experiment at SPS (Super Proton Synchrotron) CERN (European Organization for Nuclear Research). The proton rapidity distribution implies that higher nuclear stopping power is achieved in lead on lead collisions at 160AGeV/c than in sulphur on sulphur collisions at 200AGeV/c. The measured transverse mass distributions of hadrons (pions, kaons and protons) are found to be well described by a hydro-dynamical model with a single freeze-out temperature and a transverse flow velocity for each colliding system. Transverse flow at the central rapidity is seen to be increasing with the size of the colliding system from sulphur on sulphur collisions to lead on lead collisions. Two particle interferometry measurements with sulphur on lead collisions show that the transverse extension of the particle source is similar for pions with higher transverse momentum (and hence without suffering from any resonance effect) and kaons, suggesting the similar freeze-out volume for all hadrons. A scenario for the evolution and the freeze-out of the interaction region during the high-energy heavy-ion collisions is speculated by the above results: high baryon density caused by high nuclear stopping builds up a fire ball with a high pressure and temperature at the mid-rapidity region, then the rescattering effect creates high transverse flow of matter in the fire ball, and finally hadronization will happen at the same freeze-out time and temperature and the same freeze-out transverse volume and velocity for all hadrons.

Contents

Chapter 1. Introduction

The high-energy heavy-ion collisions in the laboratory at BNL (Brookhaven National Laboratory) and CERN (European Organization for Nuclear Research) in 1986 have triggered to explore a new state of matter, called Quark Gluon Plasma (QGP). Quantum Chromo-Dynamics (QCD) calculations predict that at very high energy densities above a few GeV/fm^3, matter undergoes a phase transition to QGP. At low energy densities, quarks and gluons are bounded by the strong force into colorless objects, the confined hadrons. In addition, quarks acquire a large effective mass ($m_u \approx m_d \approx 300$ MeV, $m_s \approx 500$ MeV) via interactions between themselves and the surrounding physical vacuum as a result of chiral symmetry breakdown. When increasing the energy density by increasing the temperature (heating) or by increasing the matter density (compressing), the phase transition to QGP will occur and the true perturbative vacuum of QCD appears, where partons are deconfined and chiral symmetry is approximately restored ($m_u \approx m_d \approx 5$ MeV, $m_s \approx 150$ MeV). As seen from the phase diagram shown in figure 1-1, the early universe presumably underwent this phase transition 10^{-5} seconds after the Big Bang. Critical phenomena which were expected to occur close to a phase boundary, for example long range density fluctuations, might have a bearing on important aspects of cosmology, such as nucleosynthesis, dark matter, and the large-scale structure of the universe. In astrophysics, the dynamics of supernova explosions and the stability of neutron stars (density $\rho \approx 10\rho_{nucleus}$) depend on the compressibility and the equation of state of nuclear matter, and even a possibility is discussed that the core of neutron stars consists of cold QGP. The study of extreme states of matter created in high-energy heavy-ion collisions provides us an opportunity of gaining insight into many important aspects in different fields of physics [1-1].

The figure 1-2 shows a streamer chamber picture of a heavy-ion reaction (200 AGeV/c sulphur on gold) measured in NA35 experiment at SPS CERN. The resulting mess looks very much like an experimentalist's nightmare, hundreds of final-state particles widely distributed with no discernible structure besides the purely kinematic concentration at small angles with respect to the beam direction. Because of the rapid evolution, experimental observable will be an integral over the complete space-time history of the reaction from the first nucleon-nucleon collision until freeze-out. Resulting that disentangling the various contributions to a signal from the different phases indeed presents a formidable challenge. We try to find simplicity in the apparent chaotic final states of A-A reactions applying macroscopic and statistical concepts: from particles to statistical ensembles described by non-perturbative QCD thermodynamics in terms of macroscopic variables such as pressure, temperature and volume.

In order to have a clear picture on the initial stage of the heavy-ion reactions and the succeeding evolutions, various observables in the final state are measured and analyzed on the basis of simulation calculations. In NA44 experiment, single particle momentum distributions and two particle interferometry for hadrons are studied with 450GeV/c proton, 200AGeV/c sulphur and 160AGeV/c lead induced

reactions on to the several different target nuclei. The rapidity distributions can be used as a tool to measure the energy density, and transverse momentum distributions are used for measuring the temperature by assuming the thermalization of the system. Intensity interferometry is a technique pioneered by Hanbury-Brown and Twiss to measure the size of giant stars by optics means. This technique is now used to measure the space-time evolution of the heavy-ion collision by detecting two identical particles simultaneously, the so-called two particles interferometry. The aim of this thesis is to do the high-energy heavy-ion experiment, and to analyze the measured data to extract the physical distributions, then to compare the data with the model calculations (micro-scopic cascade model RQMD and hydro-dynamics) to make interpretations to the experimental results and to understand dynamical evolution which can not be known from the experimental measurement of the final freeze-out stage of the collisions, finally as a result of the above procedures, a scenario of evolution and freeze-out of fire ball in the high-energy heavy-ion collisions by using the both single particle distributions and two particle interferometry with identified hadrons in NA44 experiment at SPS CERN.

One example of calculation from RQMD is shown in the figure 1-3 in order to know the dynamical evolution. The figure shown here is 'light cone' presenting the produced position longitudinal to the beam direction and the produced time measured in the nucleon-nucleon center-of-mass frame of pions in 160 AGeV/c Pb+Pb collisions to visualize the space-time evolution of the colliding matter.

Figure 1-1: phase diagram for QGP

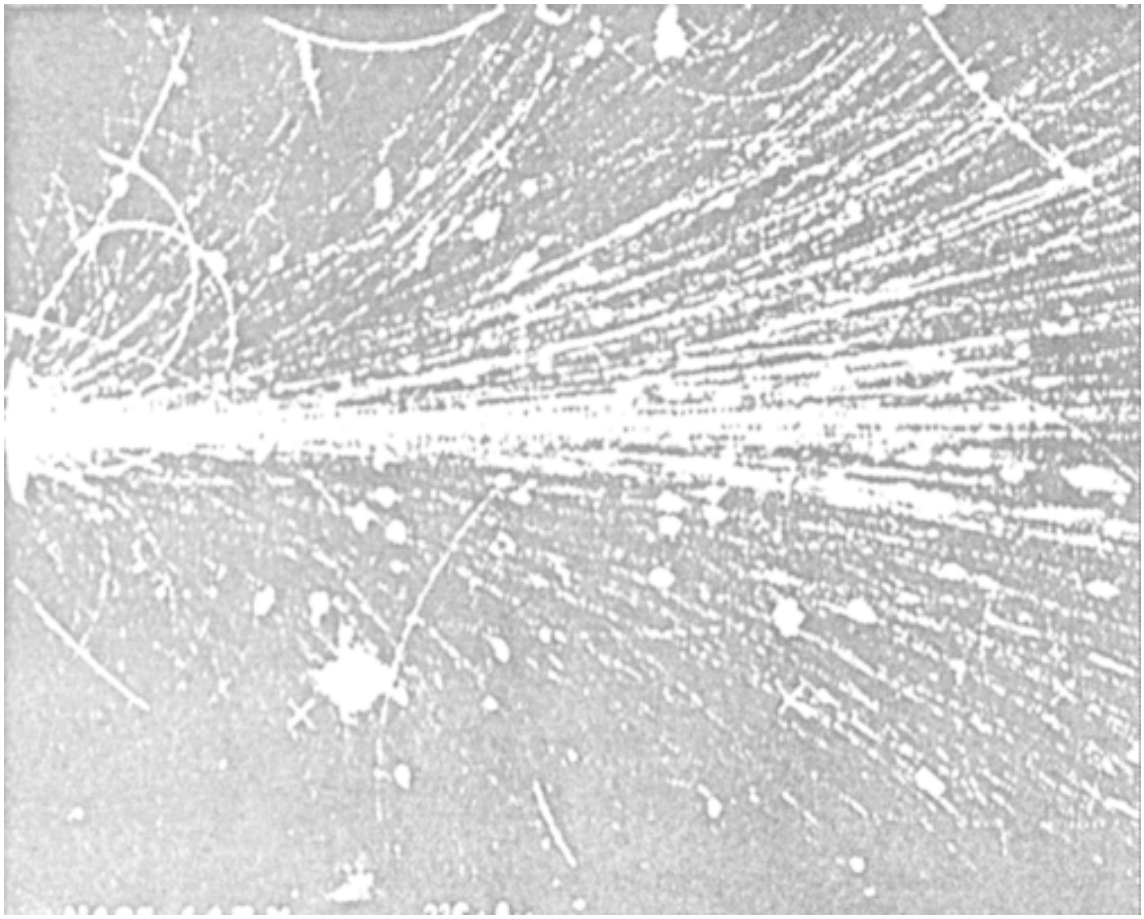

Figure 1-2: 200 AGeV/c sulphur on gold collision

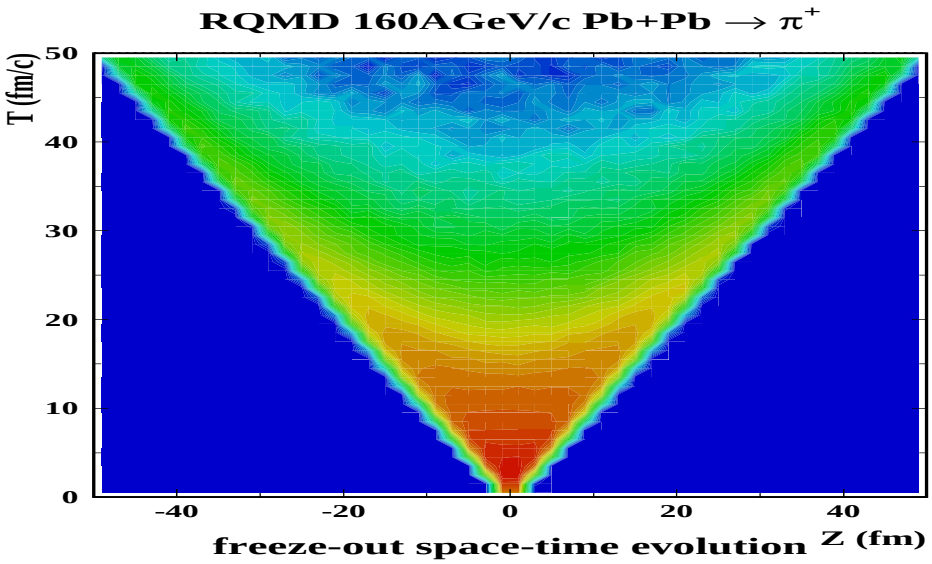

Figure 1-3: light cone created by RQMD event generator

Chapter 2. NA44 Experiment

2.1 Overview

NA44 experiment is one of the fixed target experiment using heavy-ion beams accelerated by the Super Proton Synchrotron (SPS) at CERN. 450GeV/c proton beam, 200AGeV/c sulphur beam and 160AGeV/c lead beam were used in this experiment with beryllium, sulphur, silver and lead targets in order to do the systematic study of the high-energy heavy-ion collisions. The NA44 focusing spectrometer is optimized to measure single and two particle distributions around the mid-rapidity in order to investigate the single particle productions and the space-time evolution of the colliding system with the two particle interferometry of hadrons [2-1,2,3,4].

This focusing spectrometer is shown in the figure 2-1, and consists of two dipole magnets for selecting particle momenta and three quadruple magnets to focus the secondary particles on the following detectors. By changing the current of the magnets and moving the spectrometer angle, the transverse momentum acceptance is covered up to around 1.5 GeV/c for pion, kaon and proton at around the mid-rapidity ($2 < y < 4$). Three scintillation hodoscopes [2-5] are used for tracking and time of flight measurement combining with Cherenkov beam counter [2-6]. The momentum resolution of this system is $\Delta P/P = 0.2\%$, time of flight resolution is σ_{TOF} = 100 *psec*. Two threshold gas Cherenkov detectors provide the particle identification for pion, kaon and proton up to 8 GeV/c in the laboratory momentum together with the time of flight measurement. For the lead beam experiment, we added one pad-chamber, two strip-chambers, Aerogel kaon trigger Cherenkov detector and the threshold imaging Cherenkov detector in order to help the tracking and the particle identification under the high multiplicity environment. The centrality trigger is given by a scintillation counter located just after the target, where the signal of the counter is roughly proportional to the charged multiplicity. The silicon pad detector gives the charged multiplicity in the pseudo-rapidity region of $1.5 < \eta < 3.3$, which is used in the off-line analysis. For both S+S and Pb+Pb collisions, the data are corrected at top 15% central collisions.

Figure 2-1: NA44 focusing spectrometer

2.2 Target area

Beam counter is located at 0.5m upstream from the target, and consists of two identical gas Cherenkov detectors (CX1,CX2). This detector is operated with the nitrogen gas radiator in atmospheric pressure. Radiated Cherenkov photons are reflected by the flat aluminum mirror and collected by the photomultiplier tube with UV glass window. This beam counter is optimized for the heavy-ion beam. Since 200AGeV/c sulphur beam and 160AGeV/c lead beam have enough velocity to fire the nitrogen gas radiator and the number of radiated photons is proportional to the charge-square z^2 of the beam particle, therefore the photomultiplier tube gives enough resolution of the ADC signal to eliminate the different charged beam, which can be contaminated as beam fragments from the upstream interactions. The characteristic of fast timing response of the Cherenkov radiation compared with the standard plastic scintillators and fast rise-time of the photomultiplier tube give about 40psec intrinsic timing resolution of the detector. Top two figures in the figure 2-2 show the CX detector ADC spectrum and TOF difference between 2 CX detectors.

Two veto counters are located between the CX beam counter and the target to reject the beam halo and upstream interactions. The CX veto counter is a scintillation counter with 1cm diameter hole on the beam with two photomultiplier tubes reading from both sides of the scintillator. The size of the hole is changed down to 0.5cm for the Pb beam experiment to eliminate large the background. The T0 veto counter has a hole of 0.5cm diameter, is located closer to the target, and has a readout photomultiplier tube from one side. The veto counters are used in the rejection mode in on-line trigger with requiring a good hit in the CX beam counter in order to make a clean definition of the beam going onto the target.

During the beam tuning by using the upstream magnets to change the focusing size and the position of the beam spot on the target, a blade target with 1mm width is used to find the center of the target position. The focused size of the beam on the target is about 1mm in horizontal direction and 3mm in vertical direction. In the normal experimental running condition, 1cm diameter disk target is used. Because one need to have the larger area of the target than the beam spot, all beam particles should have the same probability to collide with the target nuclei in order to calculate the cross section with the beam normalization. The target thickness is selected from 1mm to 10mm depending on the target material.

The trigger scintillation counter T0 is located just after the target. The T0 counter consists of two identical scintillator pieces (1cm width, 3cm height, 0.5cm thickness) located in right and left sides of the beam with a 3mm gap in the middle. The scintillation light collection is done by two light guides from top and bottom after connecting the scintillator pieces. Two photomultiplier tubes are attached to the both end of the light guides. The amount of the signal from the T0 scintillation counter is roughly corresponding to the number of the charged particles going through the geometrical acceptance of the T0 counter, which covers around back-

ward pseudo-rapidity region. Therefore this counter is used in the on-line trigger device to determine the centrality of each collision.

The silicon pad detector is located after the T0 counter, covers backward pseudo-rapidity region ($1.5 < \eta < 3.3$), the detector is segmented into 192 pads. The detector is counting the number of charged particle in its geometrical acceptance. The data from the detector is used in off-line analysis to get the centrality of the collision.

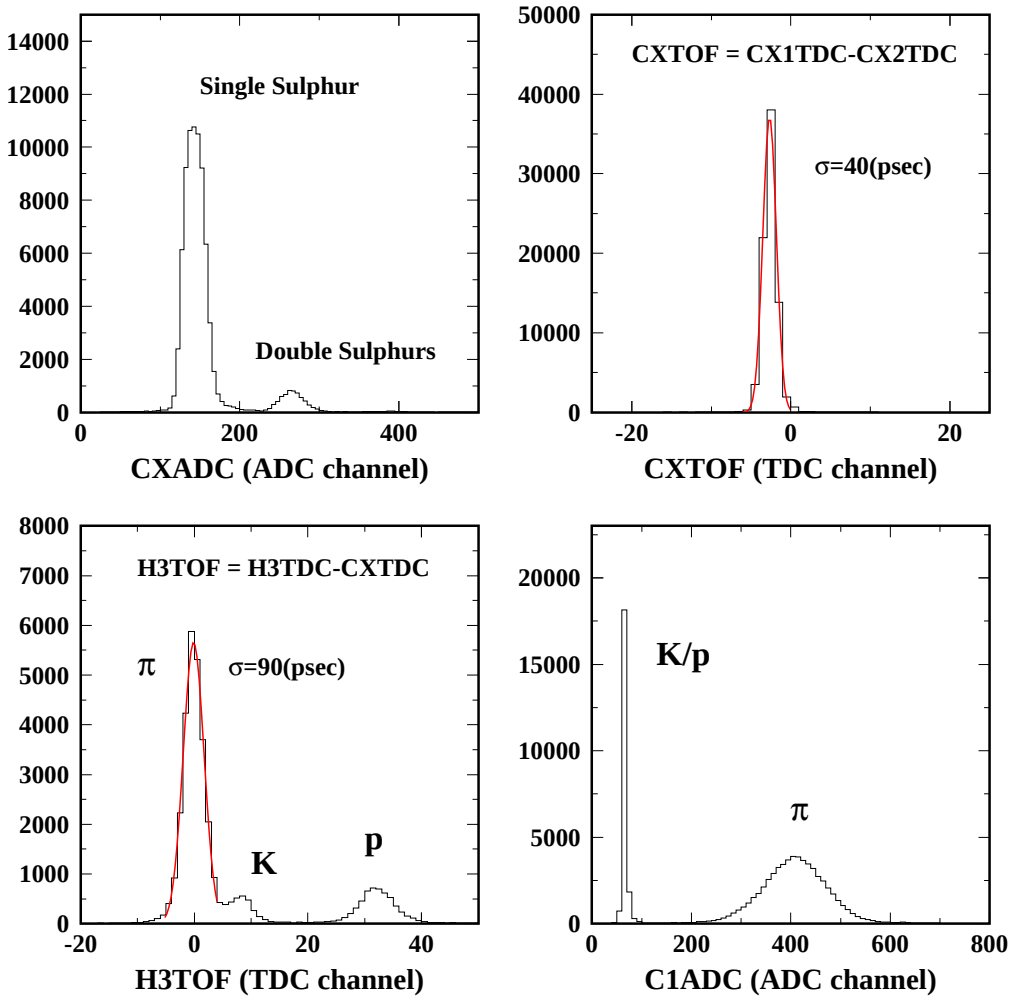

Figure 2-2: CX, H3 and C1 ADC and TOF spectra

2.3 Focusing spectrometer

First and second dipole magnets select the momentum, third dipole magnet is used for a momentum calibration with wire chambers. Three quadruple magnets focus secondary particles onto the tracking and particle identification detectors. This spectrometer is a single arm magnetic spectrometer, which has a narrow acceptance $\pm 20\%$ of the nominal momentum, therefore only the same charged particles can be measured at a time. Different charged particles will be measured by switching the polarity of the magnetic field.

By changing the currents of all magnets, the magnetic field strength can be changed to scan the different spectrometer acceptance in the space of the transverse momentum and the rapidity. To scan larger transverse momentum acceptance up to 1.5GeV/c, the magnetic spectrometer and the detectors are movable up to angle of 131mrad respect to the beam line for the 'large angle setting', while the normal spectrometer is located at 44mrad for the 'small angle setting'. The NA44 spectrometer acceptances at several settings is shown for each particle in the figure 2-3.

By changing the combination of the polarities of three quadruple magnets, the spectrometer acceptance can be changed between the 'horizontal setting' and the 'vertical setting', where two particle acceptance is different between these two settings.

Two particle acceptance is determined by a momentum difference between the two particles Q, which will be separated into the longitudinal component Q_L, which is parallel to the beam direction, and the transverse component Q_T, which is orthogonal to the beam direction. Transverse momentum difference Q_T of two particles is further separated into two orthogonal directions, Q_{TO} is parallel to the total transverse momentum of the particle pair, Q_{TS} is perpendicular to Q_{TO}. One can extract an time duration component of particle emitting source distribution with the difference between these two directions. The horizontal setting is optimized to maximize the Q_{TO} window, and the vertical setting maximizes the Q_{TS} window.

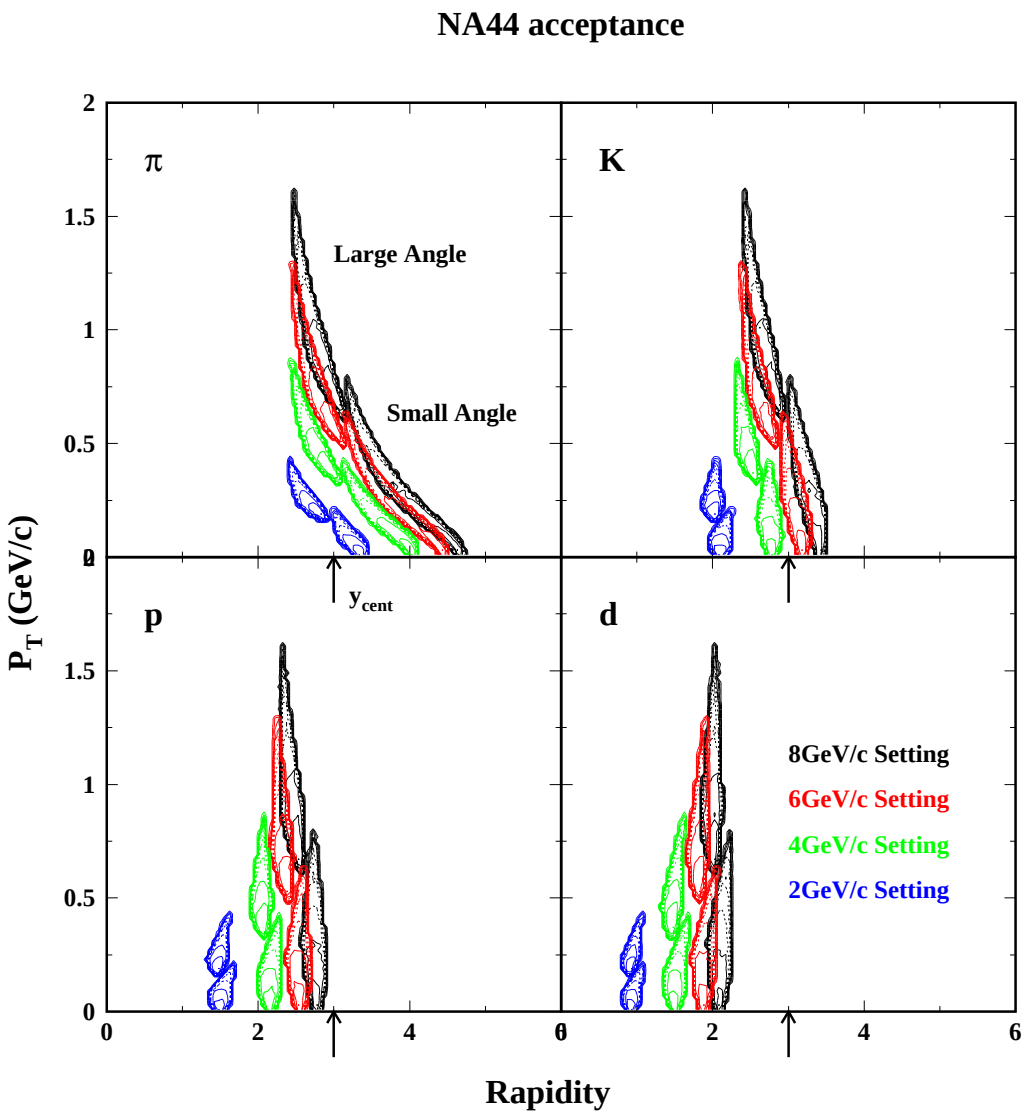

Figure 2-3: spectrometer acceptance for various settings

2.4 Tracking and TOF hodoscopes

Three scintillator hodoscopes give three 3-dimensional positions after the magnetic spectrometer in order to reconstruct the trajectories of the secondary particles in the magnetic-free space. Each highly segmented hodoscope consists of a row of 50 or 60 stick-type plastic scintillation detectors in order to know momenta of secondary particles with fine momentum resolution over a small momentum phase space described in the previous section. The specification of the hodoscope is tabled.

item	Hod1	Hod2	Hod3
elements	50	60	50
width (cm)	2.6	0.6	1.3
height (cm)	20	20	20
thickness (cm)	0.1	0.6	1.3
position (m)	10	13	18
angle (degrees)	5	90	90
X resolution (cm)	0.1	0.2	0.4
Y resolution (cm)	1.1	0.9	0.8
TOF resolution (ps)	150	130	80

The position is the distance from the target, angle is respected to a central ray of the spectrometer in horizontal plane. The each detector element has two photomultiplier tubes at both ends of the plastic scintillator. Horizontal position from the each hodoscope is given by the hitted detector element number. Vertical position will be calculated by using the timing difference between top and bottom photomultiplier tube. To calculate vertical position, one need to correct the scintillation light velocity, the difference of the rise time of the photomultiplier tubes, the timing response of the discriminator and the cable length for each element, therefore vertical offset and vertical gain are need to be calibrated. To calibrate vertical position, there are 3 horizontal scintillation counters, called finger counters, fixed at top, center and bottom of the geometrical acceptance of each hodoscope in order to make tagged events by the hits of those three counters. In off-line analysis, origin of vertical position and the scintillation light velocity inside the plastic scintillator will be calibrated in advance, using events tagged by the hits of these three scintillation counters. Momentum resolution of this system is 0.2% of the nominal momentum.

Another purpose of the hodoscope is to measure the time of flight (TOF) of the secondary particle. The TOF is calculated from the TDC difference between the hodoscopes and the CX beam counter for the heavy-ion beam experiment. On the other hand, the T0 scintillation counter is used instead of the CX beam counter for proton beam experiment. The different mass particles give the difference in TOF at the same momentum, therefore particle identification can be done combining with the measured momentum.

Because the leading-edge discriminators are used to make timing signal, the timing depends on the pulse height of the scintillation counter. Therefore both

timing information (TDC) and pulse height information (ADC) are read-out from CAMAC module for each detector element, in order to correct the effect of the pulse height dependence of the timing with 'slewing correction' technique, which will be mentioned further more in the following chapter. An intrinsic time of flight resolution of the last (H3) hodoscope is around 80psec, which is mainly used for the particle identification, because of the better separation between the different mass particles with the longest flight path. Overall time of flight resolution between CX beam counter and H3 hodoscope is about 100psec. At nominal 4GeV/c momentum setting, pion and kaon separation at H3 is around 4 sigma level in TOF. TOF spectrum between the H3 hodoscope and the CX beam counter is shown in the bottom left figure in the figure 2-2.

2.5 PID and trigger Cherenkov

Two gas threshold Cherenkov detectors are located between H1 and H2 hodoscopes. Each detector is filled with gas radiator for Cherenkov photon radiation and has a concave mirror to reflect and focus photons onto a photo cathode of a single photomultiplier tube to measure the amount of total photons emitted by particles passed through the aperture of the detector. By choosing an optimized threshold between the different particles for both Cherenkov detectors, a required particle species can be identified in on-line and off-line. Especially, rare particles can be triggered in on-line to get enough statistics for single and pair particle measurements. The first Cherenkov detector filled with freon gas radiator called C1 is fired by pions at lower pressure and is fired by pions and kaons at higher pressure depending on the nominal momentum setting. The second Cherenkov detector filled with nitrogen gas radiator called C2 is fired by electrons at lower pressure and is also fired by electrons and pions at higher pressure depending on the nominal momentum setting. The C1 Cherenkov detector ADC spectrum is shown in the bottom right figure in the figure 2-2. The figure 2-4 shown here is the normalized number of photon as a function of momentum for C1 and C2 both low and high pressure setting. At 4GeV/c setting, both C1 and C2 are used at low pressure, therefore one can select pion with requiring C1 hit and rejecting C2 hit, kaon and proton can be separated by TOF. At 8GeV/c setting, both C1 and C2 are used at high pressure, pion can be selected with requiring C2 hit, kaon can be collected with requiring small pulse height in C1, because the pulse height of C1 between pion and kaon is clearly different around 8GeV/c as seen in the figure, after rejecting C1 and C2 hit, proton or heavier particles can be collected.

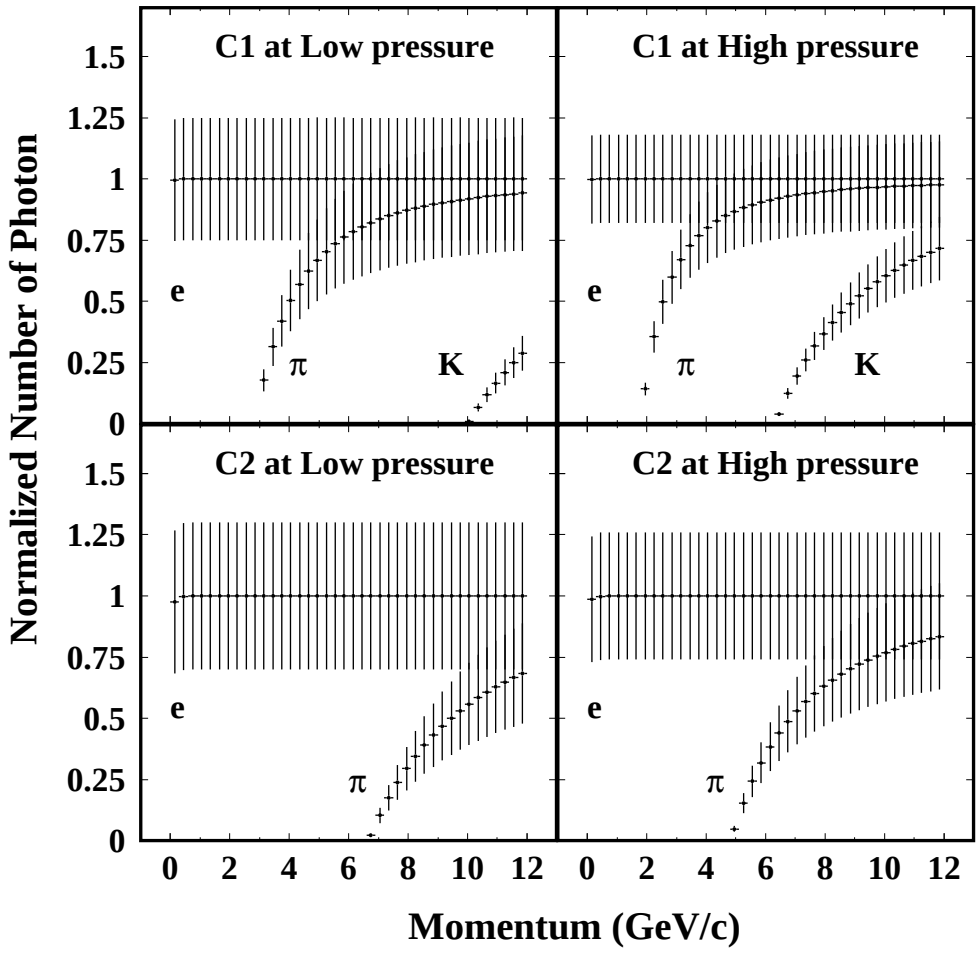

Figure 2-4: Cherenkov photon vs momentum

2.6 Trigger and DAQ

Main trigger is given by :

(1) a good beam definition (CX beam counter and veto counters),
(2) a required centrality depending the threshold of the T0 counter discriminator,
(3) at least one/two hits in each hodoscope for single/double tracks trigger selection respectively,
(4) two (C1 and C2) Cherenkov detectors trigger selection (requiring or rejecting or neglecting mode for each Cherenkov detector to select a particle species in on-line effectively).

NA44 DAQ (Data Acquisition) system is explained in this section. CAMAC (Computer Automated Modulation And Control, based on the ESONE/IEEE standard) readout and VME (Virtual Memory Extension) bus network and IBM tape driver are controlled by a Macintosh computer (32 bit 68040 CPU running at 40 MHz) to flow the data from CAMAC into VME and tape driver and to write the data onto an IBM tape. A tape writing speed is 200 Kbytes per second, For given burst of 10^7 sulphur ions, 400-500 single particle triggered events are written to the tape. The typical event size is about 800 4-byte integer words. 60,000 events per tape are written as one run corresponding to 200 Mbytes. Several monitoring Macintosh is looking for the data from VME to monitor and check the detector performance and data quality. To avoid false trigger from multiple beam particles, for 100 ns before and after each trigger the DAQ does not accept any triggers, this is called as before and after protection.

Chapter 3. Data reduction

3.1 Hodoscope calibration

Hodoscope is a device to measure positions of the track trajectory and time of flight from the target. To get those informations, several steps of calibration are necessary. There are five steps of the hodoscope calibration called PASS1, PASS2, PASS3, PASS4 and PASS5.

In PASS1, ADC pedestals of all photomultiplier tube will be calibrated with non-hitted (no valid TDC signal) detector elements (slats) from each event. The fitted pedestal peak values will be saved as a calibration constant called 'PEDE'. The time of flight TOF peaks are calculated.

$$TOF = \frac{TDC(top) + TDC(bottom)}{2} - \frac{TDC(CX1) + TDC(CX2)}{2},$$

which is the time difference between the hodoscope and CX beam counter. The peak for each slat is fitted and saved as 'TOF1'. A velocity of scintillation light within the slat will be calibrated, a timing difference $TDF(i)$ between top and bottom photomultiplier tubes in one slat will be calculated for three different event groups requiring a hit of one of the three horizontal slats, called 'finger counters'.

$$TDF(i) = TDC(top) - TDC(bottom),$$

where i is 1,2 and 3 corresponding top, center and bottom finger counter, respectively. Timing difference of these three $TDF(i)$ and real Y position $Y(i)$ of those three finger counters give the Y position gain parameter Y_{GAIN} with the following formulas,

$$Y_{GAIN}(i,j) = \frac{Y(i) - Y(j)}{TDF(j) - TDF(i)},$$

$$Y_{GAIN} = \frac{Y_{GAIN}(1,2) + Y_{GAIN}(2,3)}{2},$$

which is proportional to the scintillation light velocity inside the slat, called 'TDIF' and 'YVEL' constants. This Y_{GAIN} calibration is done with special calibration run 'finger counter run' to get enough statistics of finger counter hitted events, where at least one hit of the finger counters will be required in on-line trigger to take the special calibration run. Because this Y_{GAIN} parameters are rather stable, this calibration is done once in one period of the beam time.

In PASS2, a pulse height dependence of the time of flight will be corrected, this correction is called as a slewing correction. Because the leading edge discriminator is used for timing information, the pulse height dependence of the time of flight is well known as the following formula,

$$TOF = A + \frac{B}{\sqrt{ADC}}.$$

This is an effect that smaller charged pulse firing the leading edge discriminator give more delaied output timing signal than larger charged pulse, because of a characteristic fixed rise time of the photomultiplier tube and a fixed threshold of the leading edge discriminator. Two dimensional histogram (TOF vs ADC) will be fitted with the formula to get the parameters A and B and saved as 'SLEW' constants.

In PASS3, the same previous 'slewing correction' will be done again, to tune the slewing parameters finely. Only one time of the slewing correction is sometimes not enough or over corrected, therefore this correction will be done twice. Then the reviced slewing correction factor 'SLEW' constants will be saved.

In PASS4, the corrected time of flight offset with the 'SLEW' constants will be fitted in order to move the fitted peak into $TOF = 0$. Normally, the highest peak will be fitted for pion triggered run, since the pions are normally major particle and will make the highest peak in every slats at each hodoscope. In case of kaon/proton triggered run with C1 and C2 on-line selection, the earlier or later peak in TOF spectrum can be chosen by an external flag to force the fitting of the peak of kaon or proton for the TOF offset correction. Because the ratio between the amounts of kaons and protons is closer compared with the amount of pions, and depends on the slat number on each hodoscope, which is corresponding the particle momentum and TOF separation between kaon and proton is large enough to fit the specified peak. In the following analysis, this ΔTOF which is the timing difference from the main (fitted) peak will be used to calculate mass square or identify particle species. This TOF offset is saved as 'TOFS' constants. To get Y position Y_{POS} from the hit of each element slat, Y_{GAIN} which has been calibrated at PASS1 and Y_{OFF} which is the Y position offset are necessary as the following,

$$Y_{POS} = Y_{GAIN} \times (TDF - Y_{OFF}).$$

Then Y_{POS} will be known for given TDF of each hit. By requiring a hit of the center finger counter, which is located at $Y = 0$, Y offset will be calculated,

$$Y_{OFF} = TDF(2 : \text{center finger counter}),$$

and saved as 'YOFF' constants. Main peak in ADC spectrum, where the pedestal is already subtracted with 'PEDE' constants made at PASS1, will be fitted to normalize the peak ADC channel into 1 for all slats in hodoscopes, and saved as 'GAIN' constants.

In PASS5, no more constant will be made in this PASS, but a quality of the constants made in the previous calibration from PASS1 to PASS4 will be checked and shown, by looking at the several spectra and the distributions, in order to know the calibrations just made were acceptable for the coming further analysis. After the calibration, hit position and time of flight of each hit will be known for the following tracking and analysis procedures. In the figure 3-1, several output picture from PASS5 are shown. By looking at bottom two figures in the figure 3-1, one can see that the time of flight offsets are corrected for pion at zero for all slats and Y position with requiring the the hit of the finger counters shows clearly the image of the three finger counters.

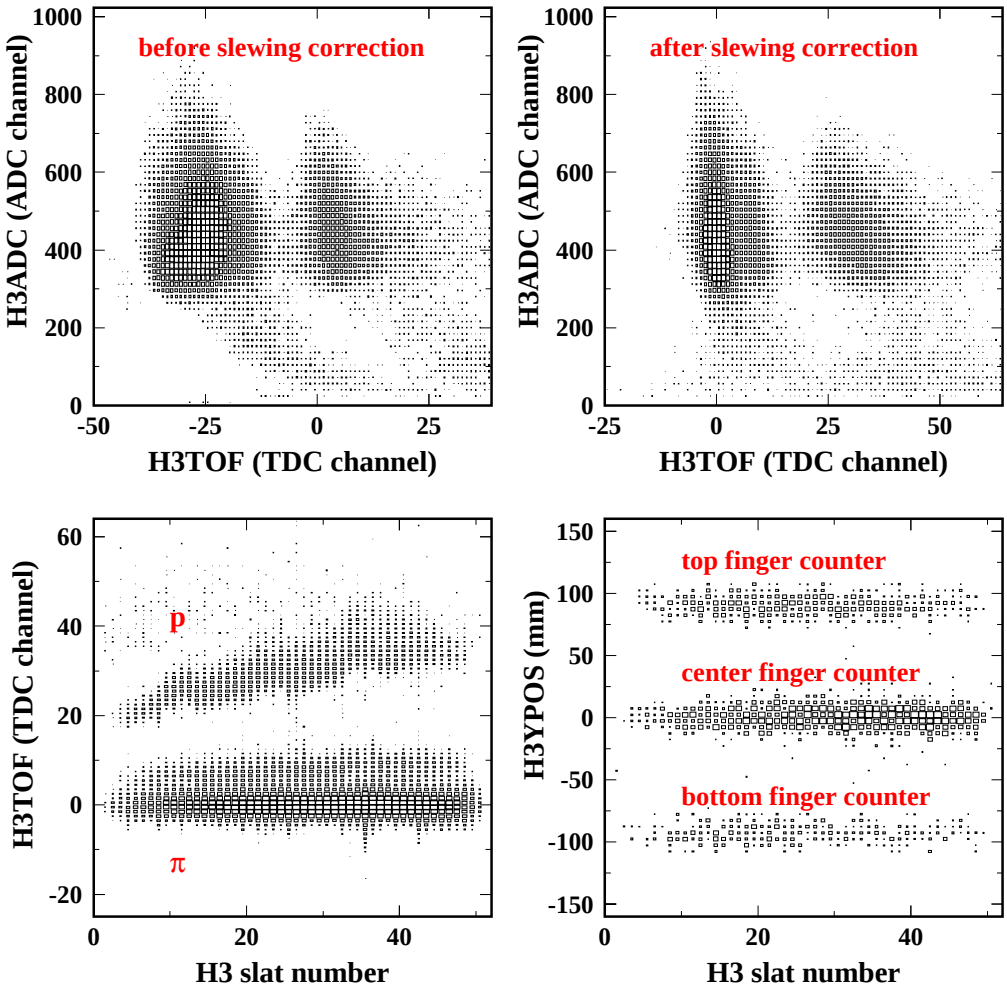

Figure 3-1: calibrated TOF and Y position

3.2 Tracking

In order to reconstruct the trajectories of the secondary particles measured by three hodoscopes, two different tracking algorithms are developed in order to check systematics and consistency. One is based on the chi-square minimizing method, another is based on look-up table.

In the chi-square minimizing method, by using the positions from the hit lists of three hodoscopes, every combinations of hits from three hodoscopes will be tried and all track candidates will be sorted in the order of the calculated chi-square value from the straight line fitting in the free space, because those three hodoscopes are located after the magnetic spectrometer, described in the previous chapter. Track candidate having the smallest chi-square will be selected. By looking at the neighbouring slat hits and angle of this track, H1 ADC pulse height will be checked whether the total ADC pulse height is consistent to the single track having this angle. If this is satisfied, the selected track will be defined as a reconstructed track and the slats used by the reconstructed track will removed from the hit lists. Then the next smallest chi-square track will be used, until one of the three hit lists becomes empty. The hodoscope H1 is inclined 5 degrees respect to the detector axis, therefore the probability to hit neighbouring two slats on H1 is around 40% of the total number of track, this is the reason why H1 ADC pulse height is useful to separate single track and neighbouring two tracks on the hodoscope H1.

In the look-up table method, a clustering technique is used to determine single hit or double hits cluster, when there are more than one neighbouring hits cluster on each hodoscope. The hits lists of each hodoscope will be modified to the expected track hit list by taking into account total normalized ADC pulse height of each cluster. Then a track, which satisfies the three hodoscopes hit-combination found in the look-up table, is assigned as a track candidate. The look-up table is prepared by using Monte Carlo events in advance. Based on the last hodoscope (H3) hits, minimum chi-square track for each H3 hit will be normally found with avoiding the coincidental usage of the hits on the other hodoscopes (H1 and H2). But sometimes the hit combination of the maximum total chi-square for the event will be selected to maximize the total number of the reconstructed track depending on the number of the expected tracks from the raw hits and the number of the reconstructed tracks, and also avoiding the coincidental usage of the hits on each hodoscope.

Because of the difference of the treatment of close tracks between those two different tracking algorithms, tracking result is sometimes different, where the difference is around 10% of the total tracks. However, the global feature like physical spectra and momentum distributions are comparable. The figure 3-2 shows the example of the track reconstruction with three hodoscopes.

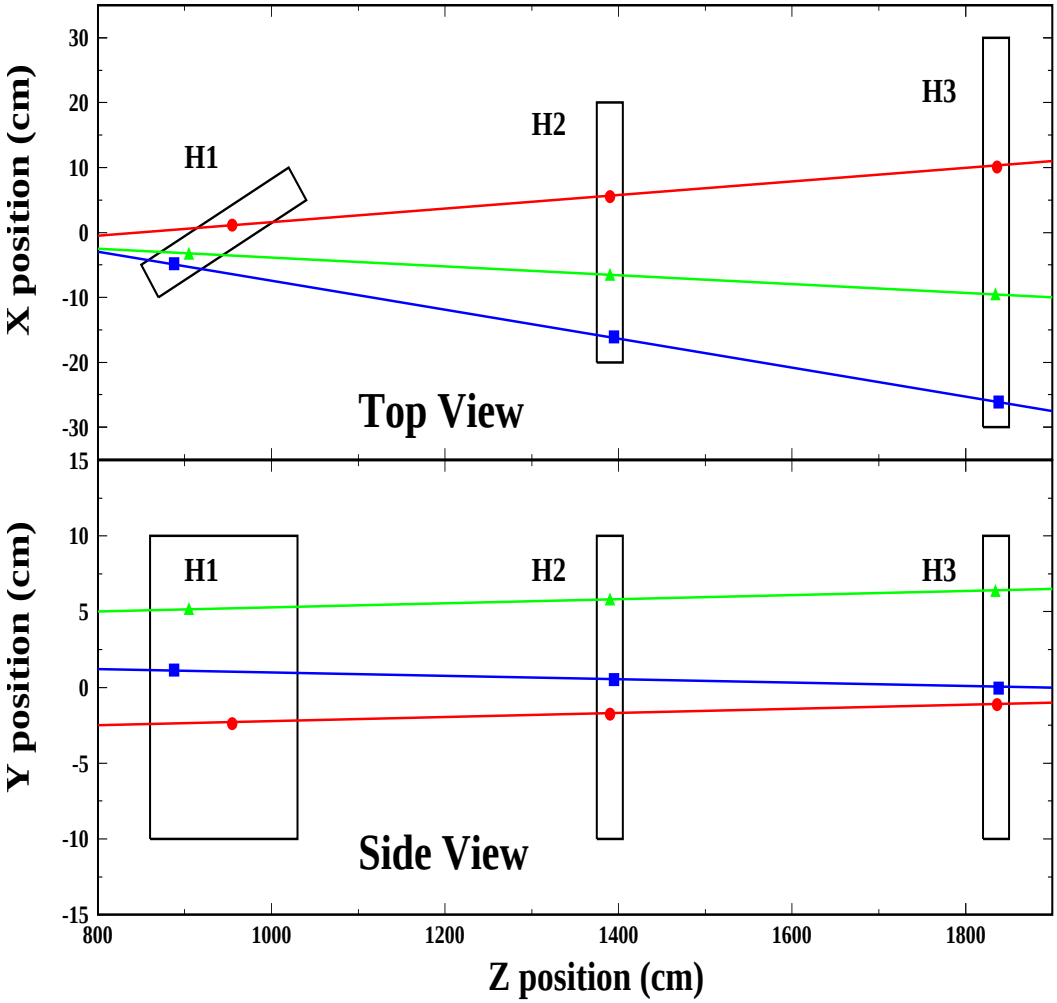

Figure 3-2: track reconstruction with three hodoscopes

3.3 Momentum reconstruction

Produced momentum at the target position for each track will be reconstructed with using the previous tracking informations. Tracking gives one position and vector at the free space after the magnetic spectrometer for each track, this position and vector will be extended backward into the magnetic spectrometer from the downstream to the upstream up to the target position in order to know the three momentum vector ($\mathbf{P}$) at the target position. Here again, two independent different momentum reconstruction algorithms are developed, one is based on a Runge Kutta method called 'ray-trace', another is based on a matrix calculation method called 'RC'.

In the Runge Kutta method, particle trajectory reconstructed by the previously discussed tracking methods will be traced back in the magnetic field map by solving a differential equation of mortion in each step until the target position. The first calculation will be done with the nominal momentum of the setting. This procedure will be iterated several times by changing the momentum until the traced back position is converged to be close enough to the real target position. Then the reconstructed momentum will be known from the final iteration. If the track does not converge onto the target, the track will be thrown away as a back-ground noise track, which does not come from the target. Track which does not go through inside the aperture of the last quadruple magnet will also be thrown away as a back-ground noise track.

In the matrix calculation method, a polynomial function approximation of the momentum as a function of the positions on the hodoscopes is first made by a look-up table of the simulated momentum and hitted positions on the hodoscopes. This look-up table is prepared with a program called DECAY TURTLE, where field matrixes of all magnets will be multiplied to the generated momentum and multiple scatterings and decaies are taken into account, in order to know the hitted slat of each hodoscope. The given polynomial function will calculate the reconstructed momentum from the hitted track positions of hodoscope H2 and H3. This method will give a fast and a good approximation.

The first methods for both tracking and momentum reconstruction are based on the experimental data, on the other hand, the second methods for both are based on the look-up table. There is a philosophical difference, the first one (chi-square based tracking and Runge Kutta based momentum reconstruction) is trying to define the noise or the back ground tracks positively to avoid the hits to be used in the other fake tracks, the second one (look-up table based tracking and matrix calculation based momentum reconstruction) is trying to neglect the noise or the back ground at the first step of the tracking to minimize the noise or the back ground hit contribution. In this case, because of low track multiplicity in the acceptance (typically one or two track in one event) and low back ground hit environment, those two approaches give almost comparable results.

3.4 data reduced file

After all processes mentioned in this chapter, compressed data file will be created for further physics analysis. There are several types of the data file, ascii or binary file having a bank structure for each process or n-tuple for a use in PAW program, which is one of CERN library, having a event and track structure will be normally used, where (1) raw ADC and TDC information for trigger devices which does not require any calibration, (2) calibrated hit positions and time of flight from hodoscopes, (3) reconstructed track informations and (4) reconstructed momentum informations will be saved into the data file.

Especially for the single particle distribution analysis, scaler informations are important to analyze an absolutely normalized cross section, therefore the scaler informations of beam and trigger devices will be recorded at the every end of burst, and those numbers are saved in the data file separately.

For the pair particle correlation analysis, further reduced file is normally prepared, after selecting good trigger or required centrality and two identical required particle species in the same event from the above data file. The new file only contains a momentums of two particle and each position of the tracking detectors to analyze two particles interferometry effect in order to analyze the large amount of the data sample efficiently. Because the positions on the tracking detector affect the analysis of the two particle interferometry, especially for pair events having small momentum difference which is corresponding to the close position on the tracking detector. This position information is used for further event selection and one needs to make the exactly same cut or selection for the fake pair event, which is created by mixing two particles from the different events.

Chapter 4. Analysis

4.1 Centrality

Centrality is characterized by the impact parameter, which is the minimum distance between centers of two colliding nuclei. This variable can not be measured experimentally, therefore total number of the secondary particle multiplicity or total transverse energy corresponding to the total number of participant nucleon are used as a tool to measure the magnitude of the collision. Total forward energy corresponding to the total number of the spectator nucleon are also used to measure the amount of energy which is not consumed at the collision. Both of those two approaches give an estimation of the impact parameter in order to know the centrality of the collision.

NA44 experiment uses one of the centrality measurement method 'charged particle multiplicity'. The T0 scintillation counter is one of the devices to measure the charged multiplicity in the backward pseudo-rapidity region. This device is also used in the trigger for on-line event selection. With requiring at least one hit of minimum ionizing particle on this device in on-line trigger, minimum biased trigger in centrality will be given. On the other hand, by triggering the T0 counter with higher threshold of the discriminator, the higher multiplicity events which means central collision will be selected. The fraction of the total hadronic cross section which corresponds to the centrality depends on the threshold value of the discriminator. In the off-line analysis, silicon multiplicity detector is also used to measure the charged multiplicity at backward pseudo-rapidity region ($1.5 < \eta < 3.3$). In the figure 4-1, correlation between charged multiplicity measured by the silicon pad detector and T0 ADC spectrum is shown for 200AGeV/c sulphur on sulphur collisions. Contour plot seen in (a) in the figure 4-1 shows the minimum bias events and solid box shows the central triggered events. A linear correlation between those two counters are clearly seen. A trigger threshold on the T0 ADC spectrum can be seen as a cut-off of the spectrum. Next two figures (b) and (c) in the figure 4-1 are projections on to those two axes, by tuning the normalization between two spectra (minimum bias spectrum and central spectrum), the centrality is calculated to be top 15% for both two projections, where 15% is a ratio hatched area from central triggered events over total area from minimum bias trigger.

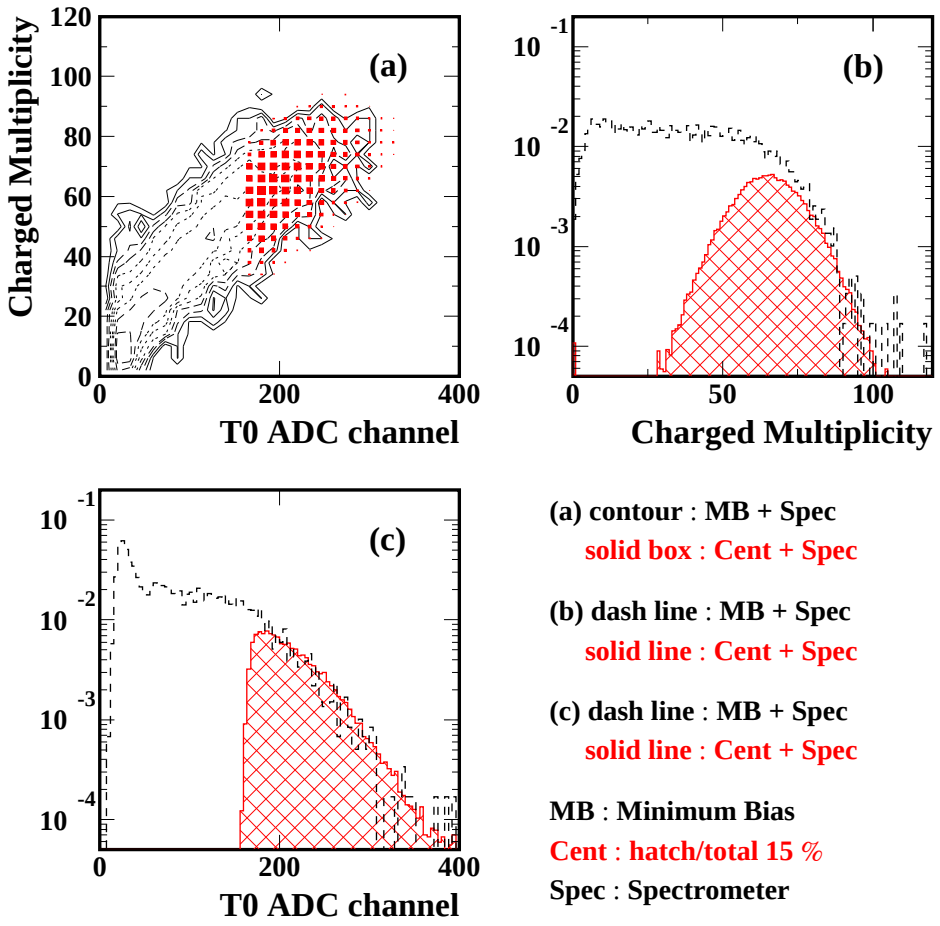

Figure 4-1: centrality measured with T0 and Silicon pad detectors

4.2 Particle identification

Particle identification is typically done with combining the time of flight measured by the hodoscopes and the two gas Cherenkov informations. The figure 4-2 shows typical example of particle identification done in the time of flight and momentum space at 4GeV/c setting. Here, Cherenkov C2 detector is already used as a veto mode to reject electrons in on-line trigger. Three bands for pions, kaons and protons can be seen clearly in (a) in the figure 4-2, however the separation between pions and kaons is not good enough to make clear particle separation. Therefore, by requiring Cherenkov C1 hit, pion is selected seen in (b) in the figure 4-2, on the other hand, kaon or more heavier particle can be selected by rejecting Cherenkov C1 hit seen in (c) in the figure 4-2.

By changing the Cherenkov gas into high pressure at higher momentum setting, for example at 8GeV/c, C1 will be fired by both pions and kaons with the different pulse height, because the clearly different velocities between pions and kaons at this momentum will make enough difference of the Cherenkov radiations between those two particles. C2 will be fired by pions, so one can also use C2 to select pion with requiring C2 hit. Proton or more heavier particle can be selected by rejecting both C1 and C2 hit. So the two Cherenkov C1 and C2 has a major role to identify pions, kaons and protons as shown in the top left figure in the figure 4-3. Proton and deuteron separation can be done with mass square given by the time of flight measurement with hodoscopes seen in the top right figure in the figure 4-3. By selecting the proper ranges of both two Cherenkov detectors C1 and C2, pions, kaons and protons are clearly separated seen in the mass square spectra shown in the bottom three figures in the figure 4-3.

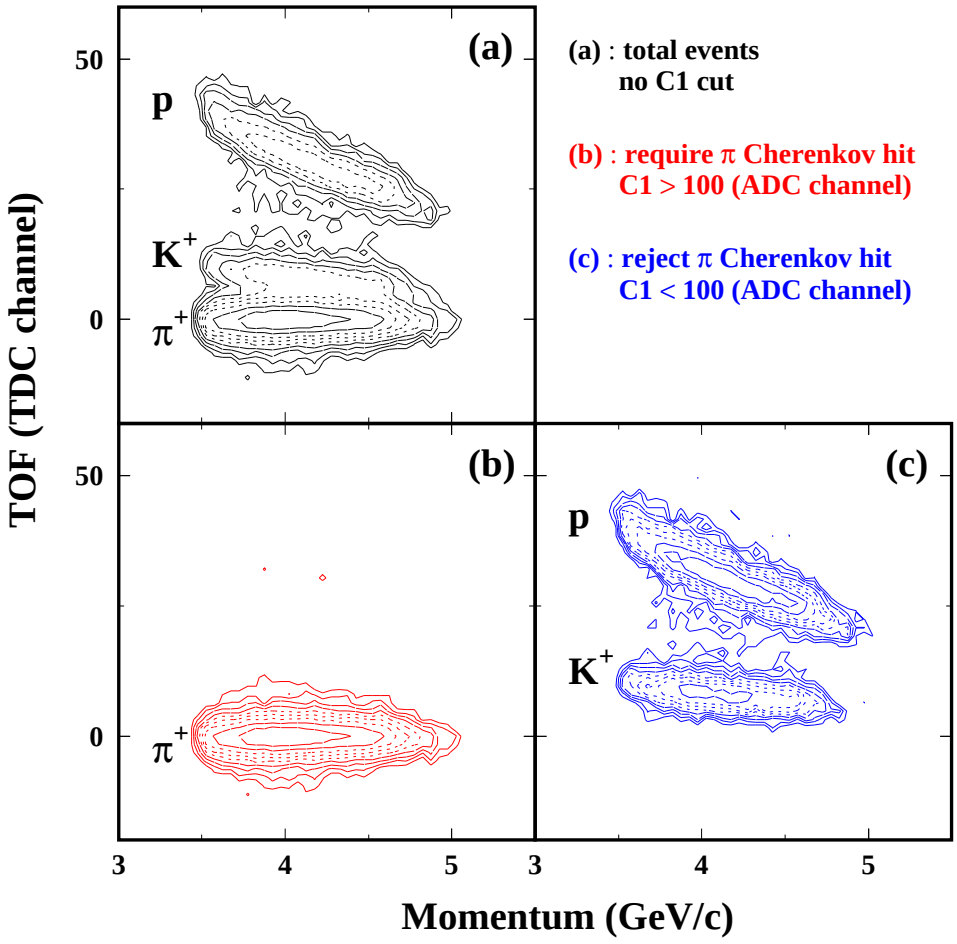

Figure 4-2: PID at 4GeV/c setting

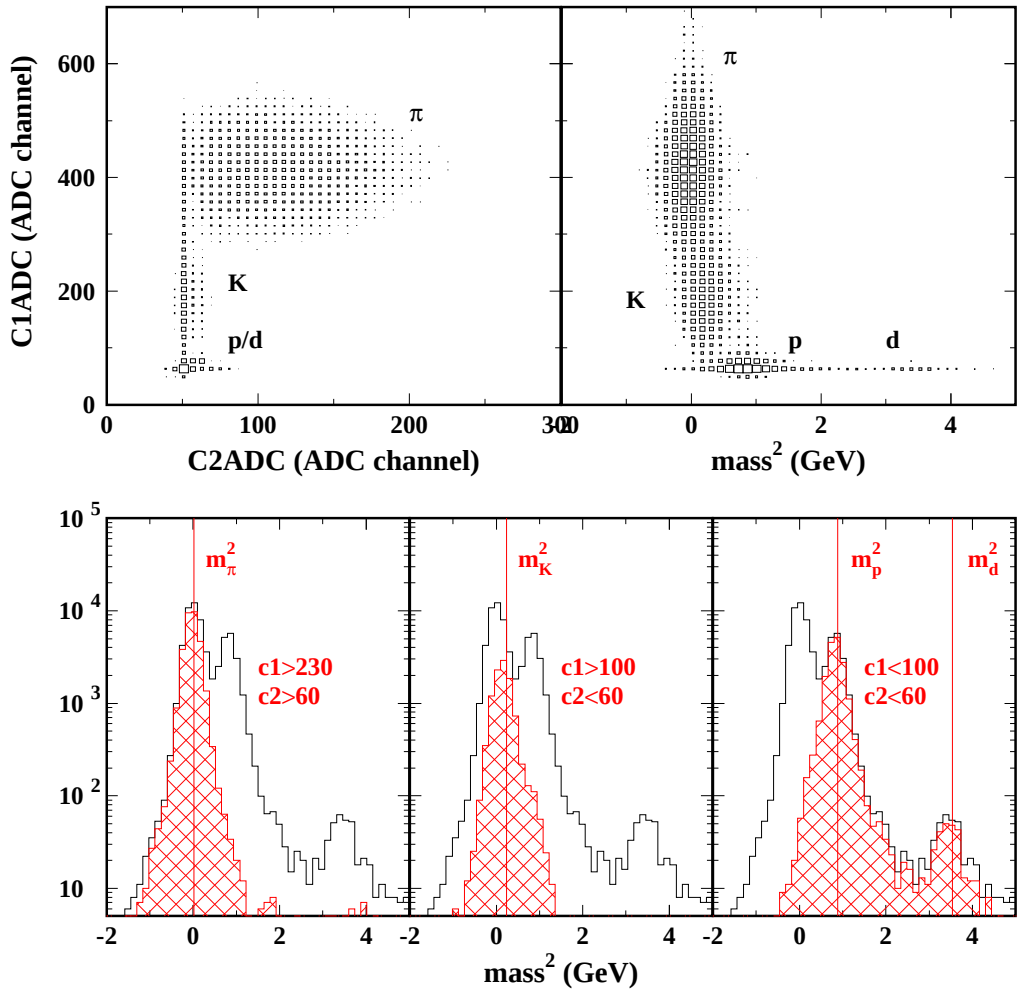

Figure 4-3: PID at 8GeV/c setting

4.3 Single particle distributions

After selecting the required centrality and the particle identification, several momentum distributions will be created. The following is the list of the necessary kinematical variables,

P : absolute momentum,

P_X : X (horizontal) component of the momentum,

P_Y : Y (vertical) component of the momentum,

P_Z : Z (beam direction) component of the momentum,

P_T : momentum (perpendicular to the beam) $P_T = \sqrt{{P_X}^2 + {P_Y}^2}$,

M_T : transverse mass $M_T = \sqrt{{P_T}^2 + M^2}$,

K_T : transverse kinetic energy $K_T = M_T - M$,

E : energy $E = \sqrt{{M_T}^2 + {P_Z}^2}$,

y : rapidity $y = \log(\frac{E + P_Z}{M_T})$,

where M is mass of the particle in question. These distributions are made from the reconstructed events accepted within the NA44 acceptance. The number of filled events are integrated over all triggered and accepted collisions during the run. For example, several single particle momentum distributions measured at large angle 8GeV/c setting for pion are shown in the figure 4-4. The measured spectra are compared with the Monte Carlo simulation, which are shown as superimposed histogram in the figure 4-4. One can see that the shape between experimental spectra and Monte Carlo are similar. The spectrum have to be corrected for the spectrometer acceptance and to be normalized to one unit collision in order to know the production of the secondary particle per collision. In the following two sections, the experimental acceptance correction will be applied and the spectrum will be normalized to one collision.

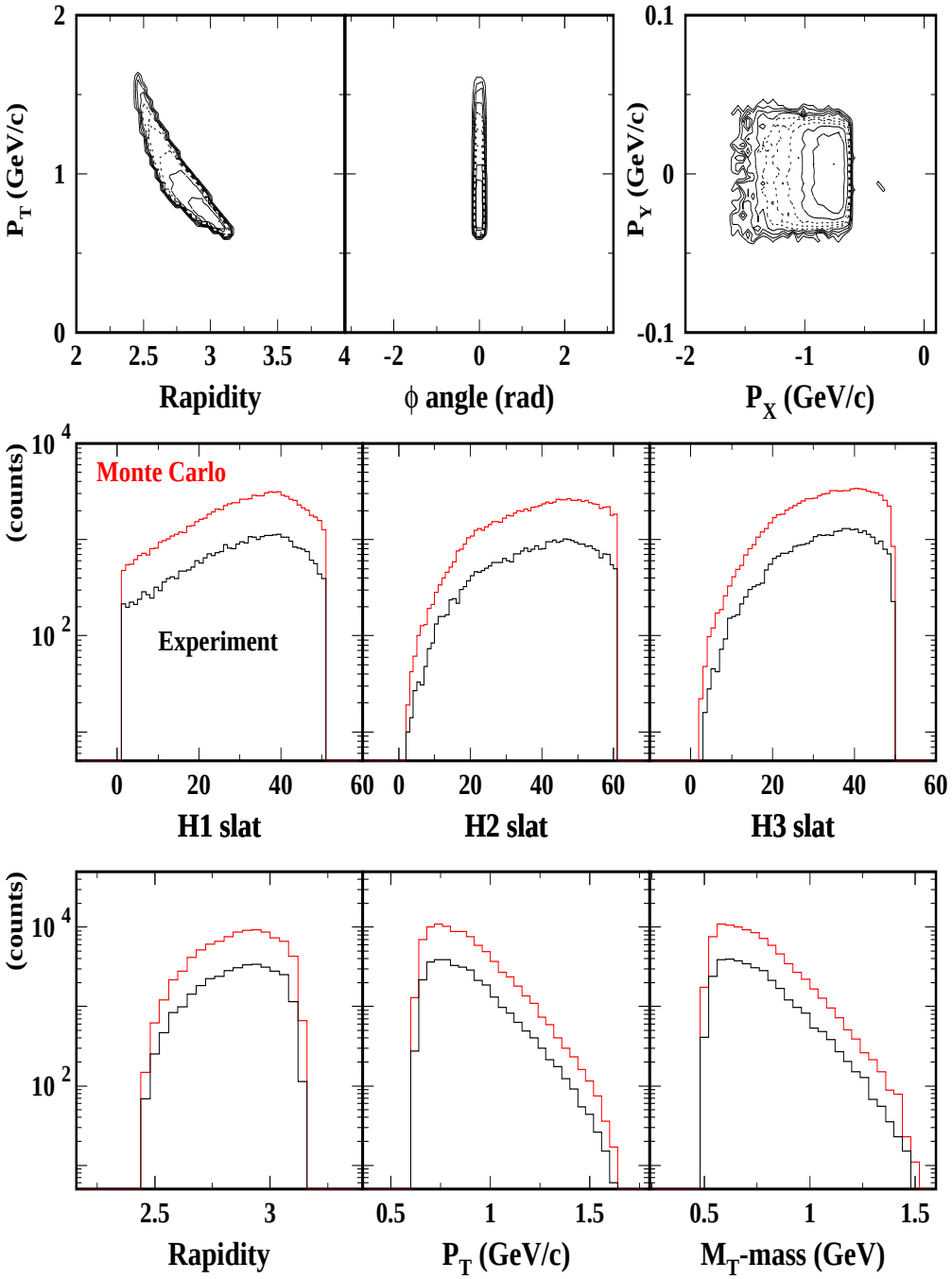

Figure 4-4: single particle distributions for both experiment and Monte Carlo

4.4 Acceptance correction

To correct the spectrometer acceptance effect to the measured spectrum, a Monte Carlo simulation is necessary. For an input momentum distribution to the Monte Carlo, a single exponential spectrum is assumed as a formula of invariant cross section $1/M_T\ dN/dM_T$ in the function of M_T, and a Gaussian shape spectrum is assumed as an rapidity distribution dN/dy for given particle species. Generated momentum spectrum is characterized as the following formula.

$$\frac{1}{M_T}\ \frac{d^2N}{dM_T dy} = \exp(-\frac{M_T}{A})\ \exp\{-(\frac{y-B}{2C})^2)\},$$

where A is an inverse slope parameter of the exponential function, B, C are a peak and a width of the Gaussian distribution, respectively. Those simulated secondary particles are transported though inside the aperture of the magnetic spectrometer with the DECAY TURTLE program, which has multiple scattering effects and decaies. By using the detector Monte Carlo program, the digitized signals on the hodoscopes are generated and recorded. Then using the digitized detector informations, the tracking and momentum reconstruction program, which has been used for the experimental data reduction, will be executed to calculate the reconstructed momentum distribution as a output from the Monte Carlo.

A definition of the acceptance correction factor CF is the ratio of a generated momentum spectrum which is an input to the Monte Carlo over a reconstructed momentum spectrum which is an output from the the Monte Carlo. This correction factor will be multiplied to an experimental momentum spectrum to get an original physical momentum distribution as following formulas. Here, the rapidity axis is already integrated to one unit of rapidity for each factor.

$$CF = \frac{\exp(-\frac{M_T}{A})\ \{= \frac{1}{M_T}\frac{dN}{dM_T}(\text{generated})\}}{\frac{dN}{dM_T}(\text{Monte Carlo output})},$$

$$\frac{1}{M_T}\frac{dN}{dM_T}(\text{corrected}) = CF \times \frac{dN}{dM_T}(\text{experiment}).$$

By fitting the corrected spectrum $1/M_T\ dN/dM_T$ with a single exponential function, an inverse slope parameter can be determined from the experimental measurement. The steps of the acceptance correction are shown in the figure 4-5. Since the exponential function $\exp(-M_T/A)$ is used as an input spectrum, the normalization of the corrected spectrum is arbitrary, so the slope parameter can only be discussed with this correction. Acceptance correction factor for the normalization will be taken into account in the following section.

Because of the shape of NA44 spectrometer acceptance which is narrower in the rapidity, especially for kaons and protons, the input parameters for the rapidity distribution such as the peak and the sigma of the Gaussian distribution will not affect

to the corrected spectrum $1/M_T\ dN/dM_T$ too much. However, the spectrometer acceptance for pion, which has strong correlation between P_T and rapidity, the corrected spectrum will depend on those input parameters. Therefore, one needs to use realistic rapidity distribution as an input to the monte Carlo particle generation at least for pion. In this analysis, the results from the other experiments (WA80, NA35 and NA49) at SPS with the same colliding system are used as the input parameters for the pion rapidity distribution in order to extract transverse mass spectra.

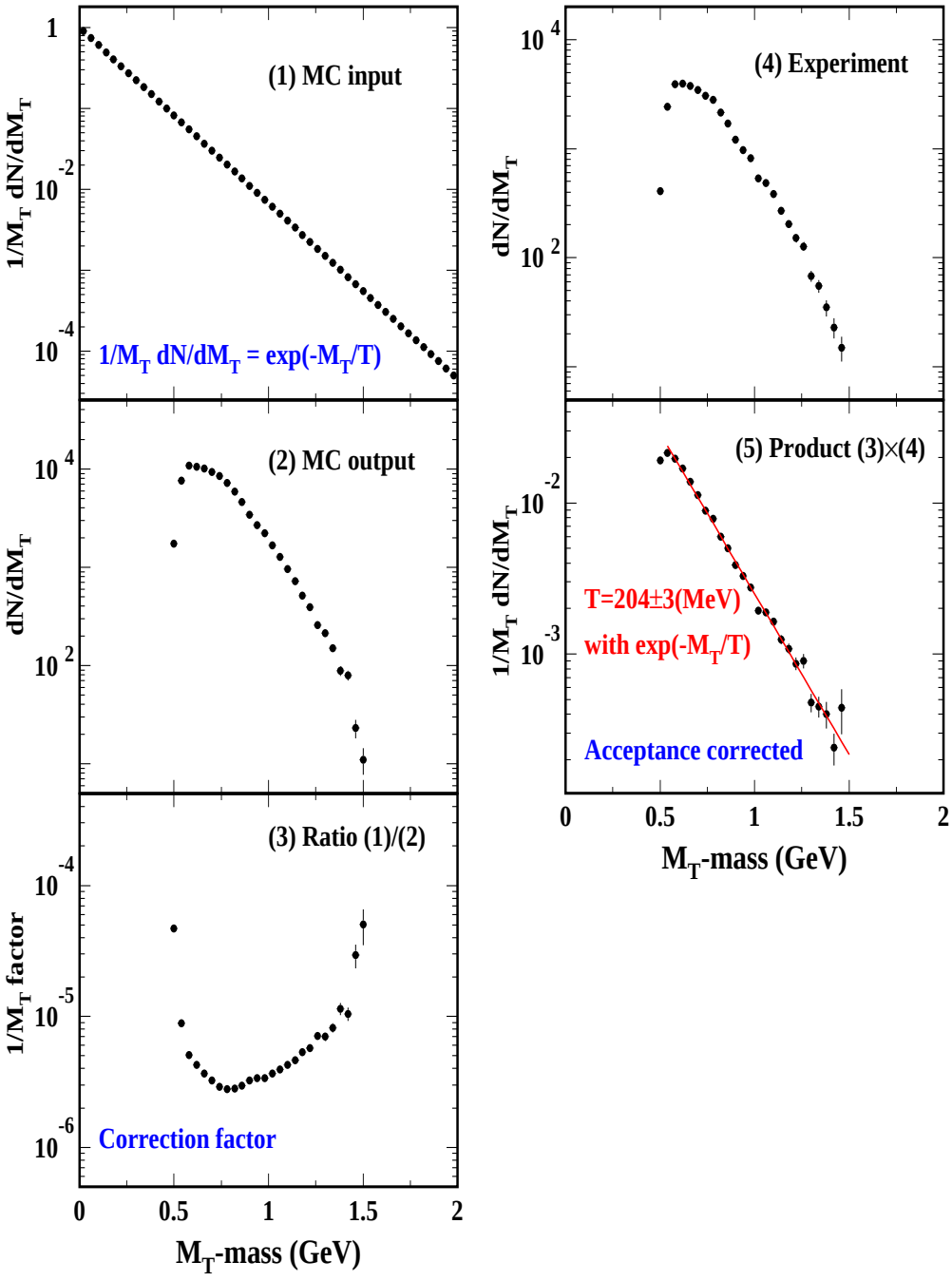

Figure 4-5: acceptance correction

4.5 Normalization

Now, an absolute production cross section, $1/(2\pi M_T)\ d^2N/(dM_T dy)$, which is normalized to one unit collision, will be calculated. The normalization factor is described as follows,

$$F = \frac{1}{N_{beam}\sigma_{int}\sigma_{trig}} \times \frac{N_{pre}}{N_{acc}} \times N_{mc} \times F_{cv} \times F_{mul}.$$

where N_{beam} is number of beam particles during the data taking. N_{pre} is the number of presented triggers, N_{acc} is the number of accepted triggers, so N_{pre}/N_{acc} gives the dead time correction factor for DAQ. σ_{int} is total geometrical interaction probability, therefore $N_{beam}\sigma_{int}$ gives the number of minimum bias collision. σ_{trig} is trigger centrality fraction, so that $N_{beam}\sigma_{int}\sigma_{trig}$ is the number of central collision for given centrality. N_{mc} is an intersection value at $M_T = 0$ of the generated Monte Carlo exponential spectrum, which is integrated over ϕ angle and normalized to unit rapidity. F_{cv} is Cherenkov veto correction factor. Kaons and protons coming through the experimental acceptance with pions or electrons in the same event will be rejected in on-line trigger, because of the on-line particle selection with the two gas Cherenkov detectors. This factor is to correct those loss in the on-line trigger selection or in the off-line Cherenkov cut and depends on the particle multiplicity and the ratios between those particles. F_{mul} is a correction factor for multi-particle event. Because the particle identification with single read-out gas Cherenkov detector can only be done for single particle event on the experimental acceptance, therefore more than two tracks events are thrown away when making the M_T distribution. This factor is to correct a fraction of multi-particle events to the single particle events. F_{cv} and F_{mul} is tabled for 4, 6 and 8GeV/c horizontal small and large angle setting with S+S collisions in the following.

angle setting	small	small	small	large	large	large
momentum setting	4	6	8	4	6	8
F_{cv}	1.17	1.24	1.35	1.04	1.03	1.06
F_{mul}	1.08	1.11	1.12	1.01	1.01	1.01

Then, multipling $F/(2\pi)$ to $1/M_T\ dN/dM_T$ given by the previous section, the absolute production cross section will be calculated in the following.

$$\frac{1}{2\pi M_T}\ \frac{d^2N}{dM_T dy} = \frac{F}{2\pi}\ \times \frac{1}{M_T}\frac{dN}{dM_T}.$$

Absolutely normalized production cross sections are seen in the figure 4-6,4-7 and 4-8 showing the several different settings at a time. By assuming the single exponential for the cross section, the exponential fitting with $A\exp(-M_T/B)$ can

be done. Using the fitting parameters A and B, dN/dy will be calculated with integrating over M_T as the following,

$$\frac{dN}{dy} = 2\pi A \int_M^\infty M_T \exp(-\frac{M_T}{B}) dM_T$$

$$= 2\pi AB \ (M + B) \ \exp(-M/B),$$

where M is the mass of the particle in question.

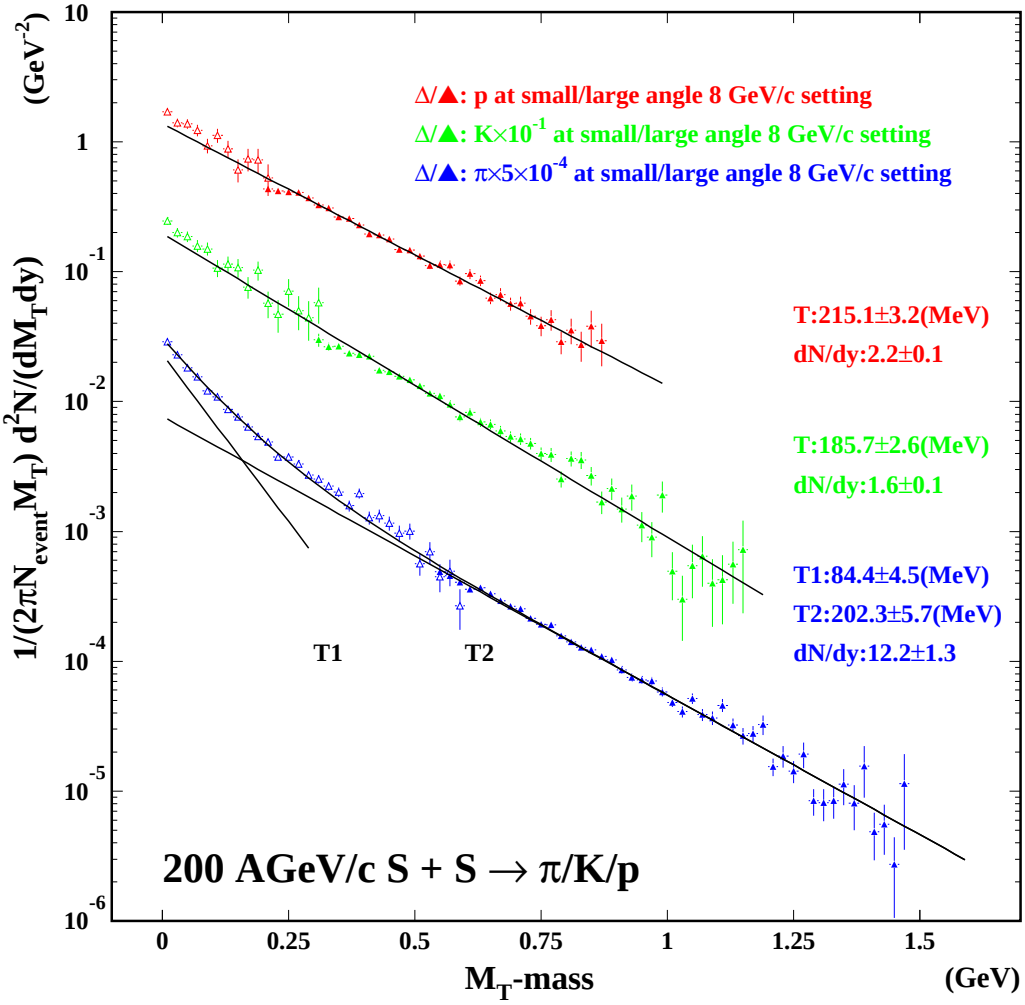

Figure 4-6: normalized production cross sections at 8GeV/c

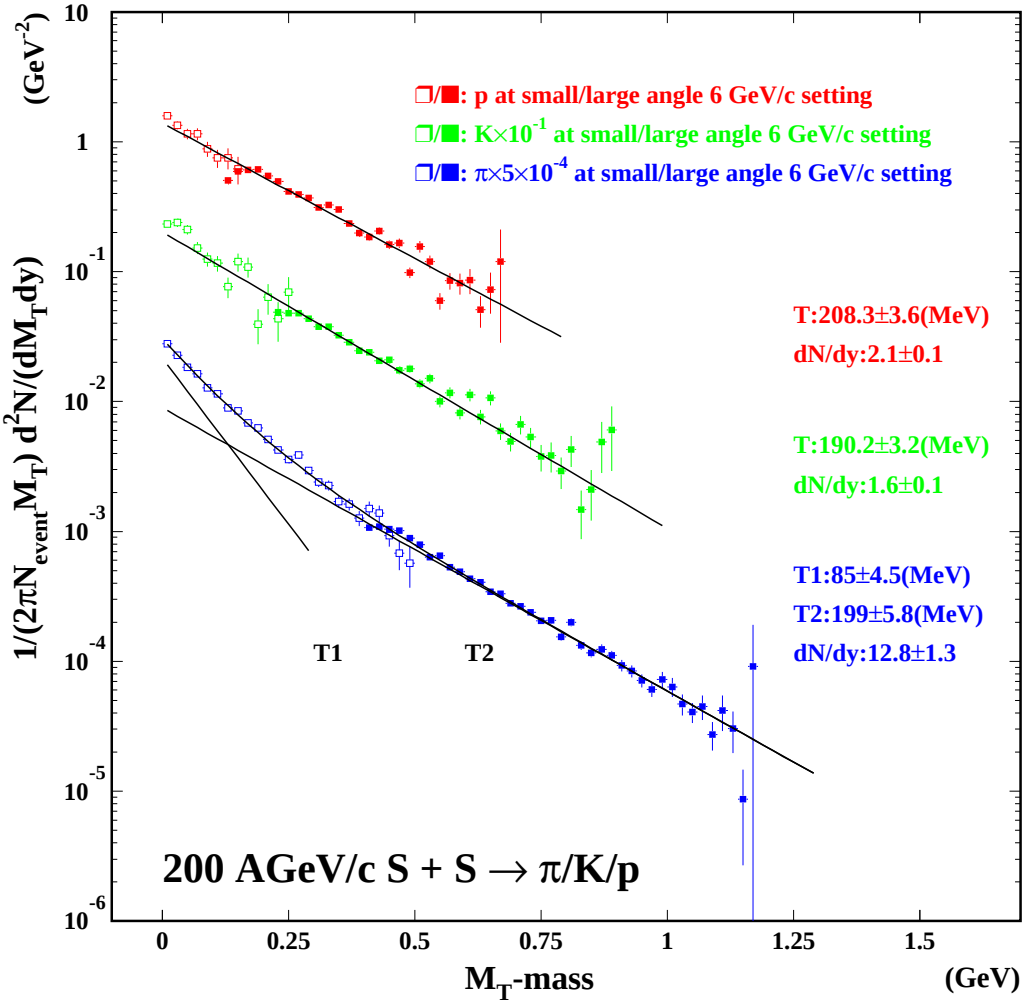

Figure 4-7: normalized production cross sections at 6GeV/c

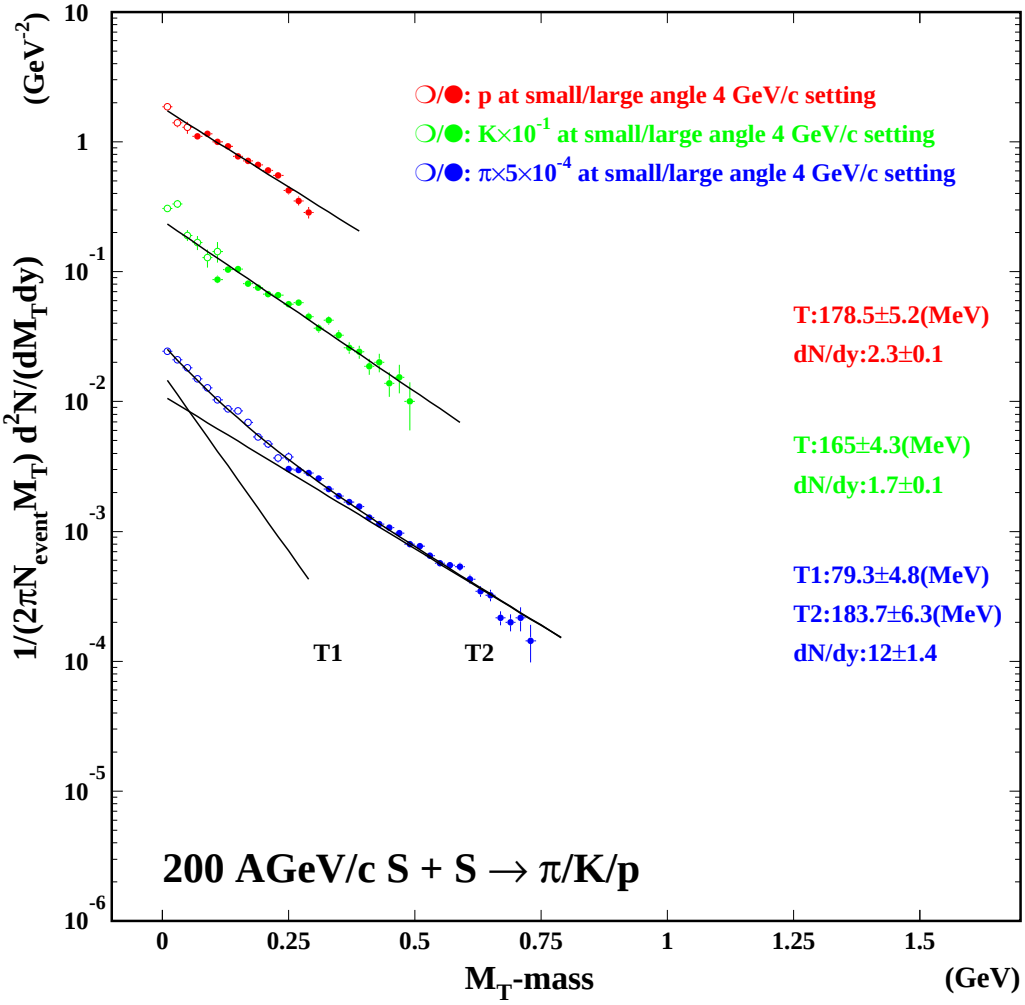

Figure 4-8: normalized production cross sections at 4GeV/c

4.6 Two particle interferometry

To study two particle interferometry, which is an enhancement at small relative momentum difference between measured two identical particles simultaneously, parameterization of those relative momentum differences is first discussed. Invariant momentum difference is defined as the following.

invariant momentum difference $Q_{inv} = \sqrt{(Q^2 - {Q_0}^2)}$

Transverse momentum difference $Q_T = \mid \vec{P_{T1}} - \vec{P_{T2}} \mid$

Longitudinal momentum difference $Q_L = \mid P_{Z1} - P_{Z2} \mid$

where $Q = \mid \vec{P_1} - \vec{P_2} \mid$, $Q_0 = \mid E_1 - E_2 \mid$, and P_Z is measured at LCMS (longitudinal center-of-mass system) flame, which the total longitudinal momentum of the two particle is equal to zero ($P_{Z1} + P_{Z2} = 0$). Q_T is separated into two orthogonal directions Q_{TO} and Q_{TS} as mentioned in the previous chapter.

Experimentally, two particle correlation function will be constructed by a ratio of a real momentum difference spectrum over a fake momentum difference spectrum.

$$C(\vec{P_1}, \vec{P_2}) = \frac{R(\vec{P_1}, \vec{P_2})}{B(\vec{P_1}, \vec{P_2})},$$

The real momentum difference spectrum $R(\vec{P_1}, \vec{P_2})$ will be filled as a function of one of the above mentioned variables, for example Q_{inv}, using two momenta $\vec{P_1}$, $\vec{P_2}$ from two track reconstructed event samples. The fake momentum difference spectrum $B(\vec{P_1}, \vec{P_2})$ is created by mixing two reconstructed momenta from two different events, here one can suppose no Bose-Einstein effect between two particles at small momentum difference in the first order approximation, therefore this fake spectrum can be used as a normalization spectrum for the real spectrum to get the two particle correlation function with the ratio of those two spectra. The correlation functions in one-dimensional as a function of Q_{inv}, and in two-dimensional as a function of Q_T and Q_L are shown in the figure 4-9.

Correlation functions will be described in the following parameterizations.

$C(Q_{inv}) = 1 + \lambda \exp(-{Q_{inv}}^2 {R_{inv}}^2)$,
$C(Q, Q_0) = 1 + \lambda \exp(-Q^2 R^2 - {Q_0}^2 \tau^2)$,
$C(Q_T, Q_L) = 1 + \lambda \exp(-{Q_T}^2 {R_T}^2 - {Q_L}^2 {R_L}^2)$,
$C(Q_{TS}, Q_{TO}, Q_L) = 1 + \lambda \exp(-{Q_{TS}}^2 {R_{TS}}^2 - {Q_{TO}}^2 {R_{TO}}^2 - {Q_L}^2 {R_L}^2)$,

where λ is a chaoticity parameter, R_{inv} is a measured source size in the Q_{inv} scale, R and τ are a geometrical source size and particles emission time duration, R_T and R_L are a transverse and a longitudinal geometrical source size, R_{TS} and R_{TO} are

a sideward source size which is purely geometrical transverse size and a outward source size which is a mixture of the geometrical transverse size and a emission time duration. Those functions are used to fit the experimental correlation function in order to extract the chaoticity and source size parameters.

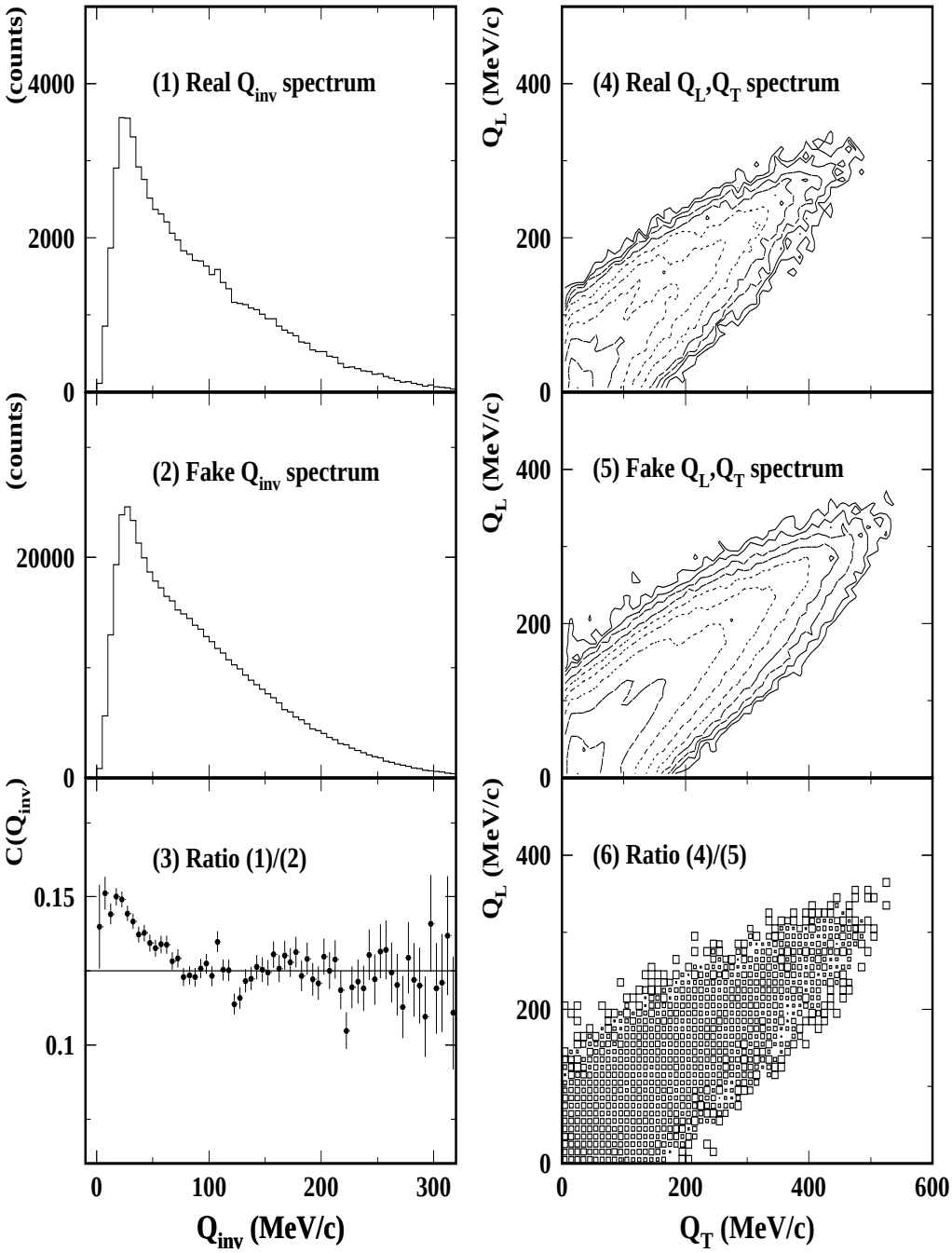

Figure 4-9: construction of correlation function

4.7 Chi-square mapping method

To extract an original correlation function, several experimental effects have to be corrected from the measured correlation function $C(\vec{P}_1, \vec{P}_2)$. Three major corrections for the measured correlation function are a coulomb correction (K_{coul}), which corrects coulomb repulsion effect especially at a small momentum difference, an acceptance correction (K_{acc}), which is an experimental detector resolution effect, a single particle correction (K_{spc}), which is a residual effect into the fake momentum difference spectrum coming from the 2 particle correlation, because of the event mixing technique using the real events. Therefore corrected correlation function can be given as follows,

$$C(\text{corrected}) = C(\text{raw}) \times K_{coul} \times K_{acc} \times K_{spc}.$$

However, those correction factors depend on the original correlation function, which will be the fitted results such as the source size and a chaoticity parameter of the corrected correlation function. To solve this parameter dependence, an iterative way of calculation will be used, until a difference between the input parameters and the output fitted results becomes negligibly small [2-4].

In this section, an approach different from the iterative way will be shown to analyze the two particle interferometry. This approach is named as a 'chi-square mapping method', where a basic idea of this approach is a comparison between an experimental data without any correction and a Monte Carlo simulated data which include every effects in order to find a best input parameter to the Monte Carlo giving the smallest chi-square between the experimental data and the Monte Carlo output data. Important points are, Monte Carlo simulation should reproduce the experiment as close as possible to the reality, the exactly same analysis procedure have to be used for the Monte Carlo events as the experimental analysis, chi-square map will be created by changing the input parameters, and the minimum chi-square will be searched to find the best input parameters as a results. The step of the approach is described in the following and shown in the figure 4-10.

Two particle events sample (typically 5 to 10 times larger than the amount of experimental data sample), where the two particles are going through the experimental acceptance, are generated, here physical single particle distribution for each particle will be assumed (exponential shape of invariant cross section in M_T and Gaussian shape in rapidity).

Those two particles will be transported into the magnetic spectrometer by the DECAY TURTLE program which has decays and multiple scattering inside and the digitized hits information of each detector will be recorded with taking into account the energy loss in the detector.

Using the digitized informations of the detectors, tracking and momentum reconstruction will be done by the same program which has been used by the experimental data analysis. Two generated momenta of generated two particles and reconstructed

momenta and the used slat number on each hodoscope of the reconstructed particles will be saved as the Monte Carlo momentum file.

Using a given set of input parameters (chaoticity parameter and radii of Gaussian source distribution) and two generated momenta of the simulated particle from the Monte Carlo momentum file, a weight which is used to decide to drop (throw away) this event or include it into the correlation function will be calculated. This weight is a product of the correlation function described in the previous section and a coulomb repulsion effect factor (which is an inverse of the Gamow correction factor in this analysis), this weight is normalized to one, where the product is maximum. The Gamow factor is shown in the following formula.

$$G(x) = \frac{x}{\exp(x) - 1} \quad : \quad x = \frac{2\pi\alpha M}{Q_{inv}},$$

which is defined as a function of Q_{inv} for given particle mass M. Then one real random number for each event will be generated between zero and one. If this random number is smaller than the weight, the event will be used to construct a real and a fake momentum difference spectra by using the two reconstructed momenta of this event, otherwise (if the random number is greater than the weight), this event will be dropped (thrown away, not used for the spectrum). The real and fake momentum difference spectra will be created with the same method as used in the experimental data analysis, especially for an event mixing method to make the fake spectrum, and for the slat cut selection to treat the neighbouring slats hit in the same way of the experimental data analysis. The correlation function is also made by the ratio of the real over the fake momentum difference spectrum in the same way. Two important points are that the generated momenta have to be used to calculate the weight and the reconstructed momenta have to be used for correlation function as an output of the Monte Carlo data to be compared with the experimental data. In this step, one Monte Carlo correlation function will be created by scanning the hole data set of the Monte Carlo momentum file with one set of the input parameters.

By changing the input parameters and doing the previous step over and over again, several Monte Carlo correlation functions will be prepared to scan those over the input parameter space. Therefore, in order to analyze one-dimensional correlation function like Q_{inv}, the Monte Carlo correlation function has to be prepared at each point of the two-dimensional parameter space in R_{inv} and λ. To find the nearest Monte Carlo correlation function to the experimental correlation function, a chi-square between the experimental correlation function and each Monte Carlo correlation function will be calculated to make chi-square map over the two-dimensional parameter space for one-dimensional correlation function with the following formula.

$$\chi^2(R_{inv}, \lambda) = \sum_{i=1}^{n} \frac{\{C(i)^{EX} - C(i : R_{inv}, \lambda)^{MC}\}^2}{\{E(i)^{EX}\}^2 + \{E(i : R_{inv}, \lambda)^{MC}\}^2},$$

where $C(i)^{EX}$ and $E(i)^{EX}$ are the experimental correlation function and corresponding error, $C(i : R_{inv}, \lambda)^{MC}$ and $E(i : R_{inv}, \lambda)^{MC}$ are Monte Carlo correlation function and corresponding error for given input parameters R_{inv} and λ, i is the bin

number, n is the total number of the bin. Therefore a chi-square map over the three-dimensional parameter space is necessary to analyze the two-dimensional correlation function like $C(Q, Q_0)$ or $C(Q_T, Q_L)$, because those function have three free parameters to be searched. Finding the minimum chi-square point in the input parameter space is done to get the best resulting fit parameters of the chaoticity and radii of Gaussian source distribution. The statistical error of those parameters are given from the region of 'the minimum chi-square + 1' as a definition.

As seen from above steps of the procedures, the effects corresponding to the correction factors, which are normally used to correct the experimental data and are mentioned as K_{coul}, K_{acc} and K_{spc} before, are included as inverses of those factors into the Monte Carlo correlation function automatically in this method. $1/K_{coul}$ can be seen in the weight for the event dropping, $1/K_{acc}$ can be seen in the distinguished usage of the generated and reconstructed momenta to create the Monte Carlo correlation, and $1/K_{spc}$ can be seen in the usage of the same event mixing method for the Monte Carlo fake momentum difference spectrum as for the experimental spectrum. The merit of this approach is that by scanning the whole parameter space to make chi-square contour map, one can know the global feature of the chi-square contour and local minimum can be found easily. On the other hand, the iteration method can be trapped by the local minimum. The demerit of this approach is that the calculation takes long time to scan over whole parameter space, so that an increase of the dimension or the segmentation of the chi-square map is not easy, compared to the iteration method. The both chi-square mapping method and the iteration method give comparable results, since there is no local minimum compare to the statistical fluctuation.

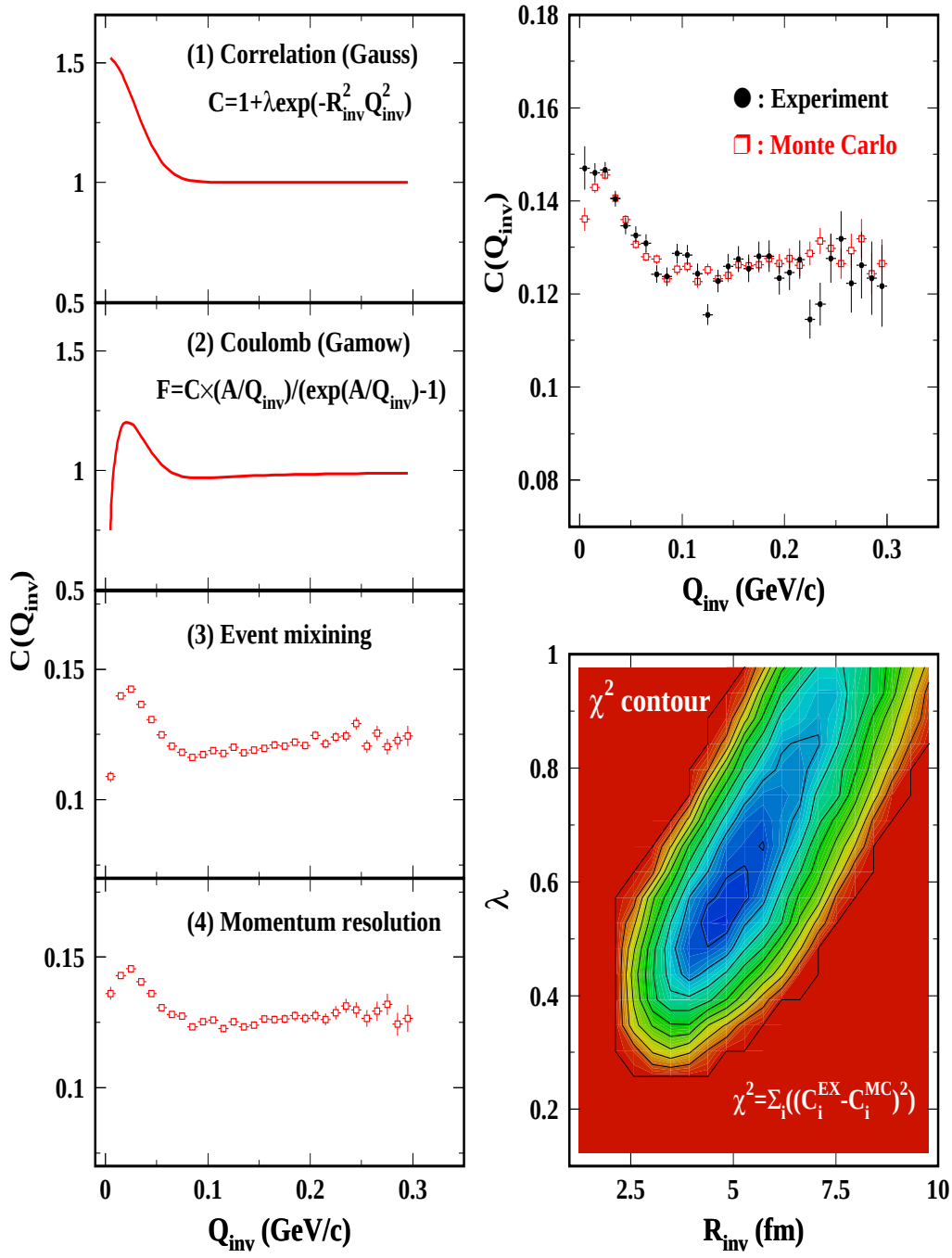

Figure 4-10: chi-square contour mapping method

Chapter 5. Results

5.1 Transverse mass spectra for pions, kaons and protons

Transverse mass spectra for identified pions, kaons and protons for both sulphur on sulphur collisions and lead on lead collisions at the central rapidity will be discussed in this section. Invariant cross sections $1/M_T\ dN/dM_T$, which was mentioned in the previous chapter, as a function of $M_T - mass$ will be shown in the figure for protons, kaons and pions from the top to the bottom in the figure 5-1, the left hand side of the figure is for Pb+Pb collisions and the right hand side is for S+S collisions. The contents described here will be focused on the shape of the distributions for the different particle species and the different colliding system. A fitting procedure to the each slope has been done with a single exponential function excluding the low P_T pions, which are well known as contaminated by resonance decaies. The fitted inverse slope parameter is seen on the top of each slope. Centralities for both systems are similar around top 15% of total geometrical cross section.

Points to be emphasized are the following. All transverse mass spectra for pions, kaons and protons for both colliding systems are well described with a single exponential function. The fitted inverse slope parameter increases with increasing the particle mass for both systems. The fitted inverse slope parameter for the same mass particle increases with increasing with the colliding system. The difference of the fitted inverse slope parameters between the colliding systems also increases with the particle mass.

The fitted inverse slope parameters are summarized in the figure 5-2 as a function of particle mass for each system. Proton on proton collisions data which is from ISR experiment [5-1] are added for the comparison. An increase of the inverse slope parameters with the particle mass, which had not seen in the p+p collisions, is clearly observed in the heavy-ion collisions. The data are fitted with the following formula as a function of mass.

$$T_m = T_f + C\beta_s^2 M,$$

where T_m is the measured slope parameter, T_f is a freeze-out temperature, β_s is a hydro-dynamical transverse surface flow velocity, M is a mass of the particle and C is a constant where we don't really know about this constant, but we here assume this constant is same for different colliding systems. Here we used $C = 0.4$ in the fitting procedure. The basic idea of this formula is that the measured inverse slope parameter is explained by two types of motion, one is random or thermal motion described by T_f, another is collective motion described by β_s. The increase of the slope parameter intuitively suggests an existence of the hydro-dynamical transverse flow of the colliding matter. An inclination of the fitted line increases with the size of the colliding system, where the inclination corresponds to the transverse flow velocity. Therefore an increase of the transverse flow velocity β_s with the colliding system is found to be $\beta_s = 0.0$ for p+p, $\beta_s = 0.4$ for S+S and $\beta_s = 0.5$ for

Pb+Pb collisions. An intersection of the fitted line of the inverse slope at mass=0 is corresponding to the freeze-out temperature T_f, which is found to be around 140 ± 15 (MeV). The results shown here suggest a scenario that secondary particles freeze out at the same temperature, and this freeze-out temperature does not increase with increasing the colliding system too much. This is a signal that a thermalization might be already achieved locally around the central rapidity region at SPS energy.

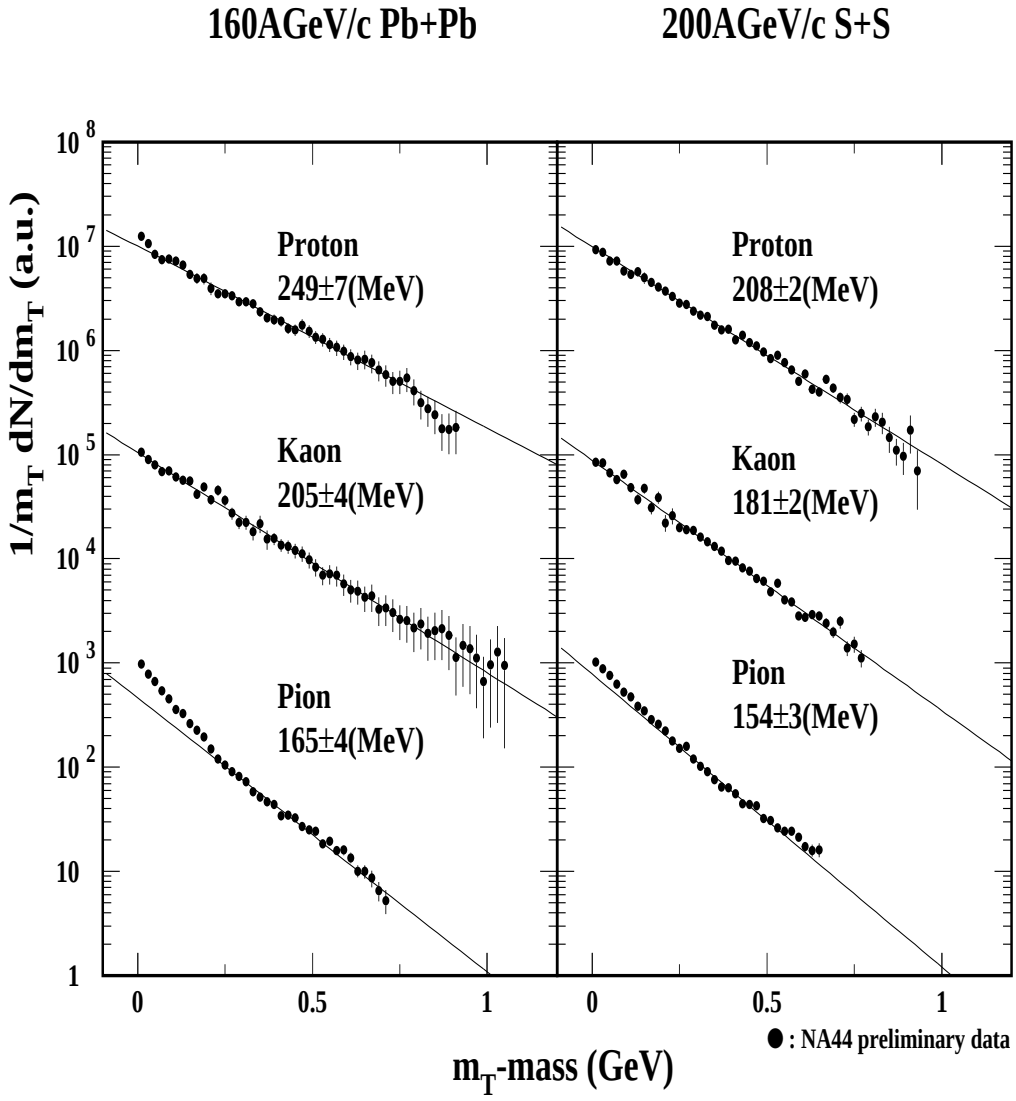

Figure 5-1: transverse mass spectra for hadrons

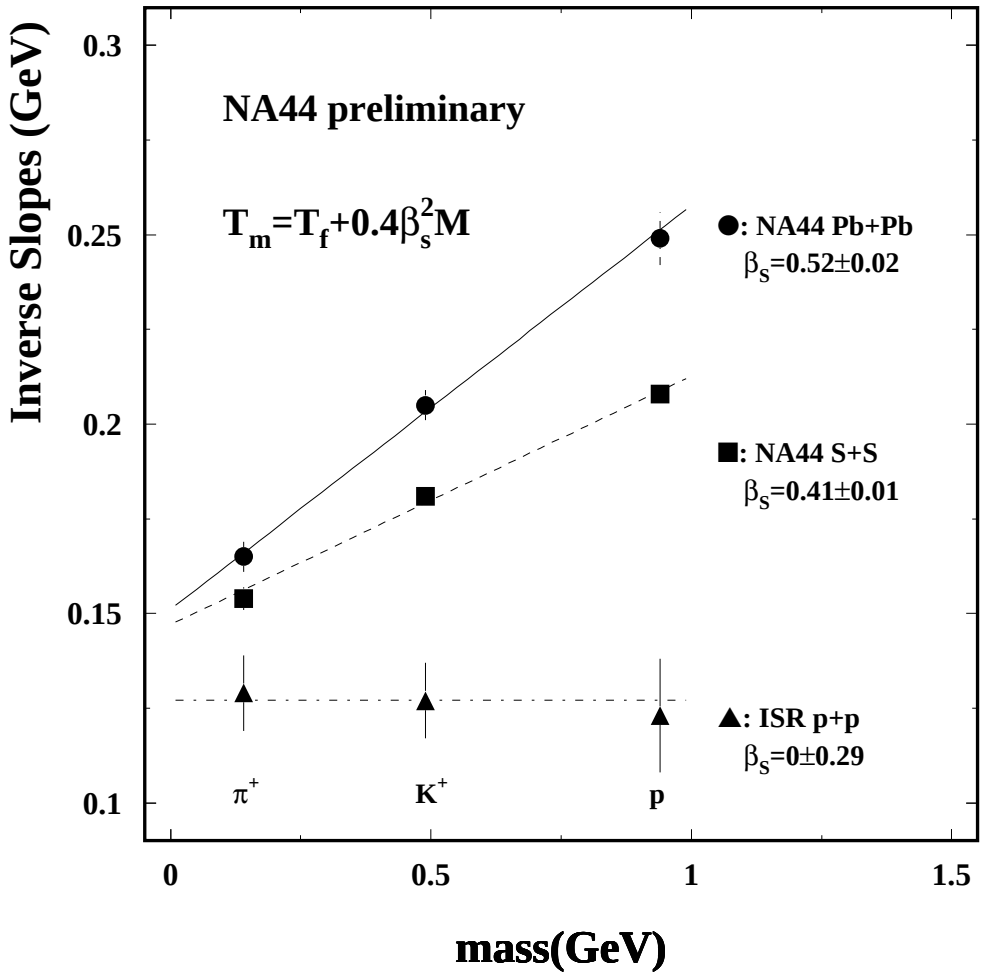

Figure 5-2: summary of inverse slope parameters

5.2 dN/dy for pion

By integrating the absolutely normalized invariant cross section over M_T, dN/dy for pion is calculated to be 12.4 $\pm$ 0.8 for S+S collision and 89.5 $\pm$ 9.5 for Pb+Pb collisions. Because pion M_T slopes are clearly curved, a single exponential function can not explain the spectrum. Therefore, for both systems, two exponential components are assumed. The fitting of two exponential functions is seen in the figure 5-3 and the fitted functions agree with the experimental spectra rather well. The shape of two distributions are similar, although the colliding system is completely different from S+S to Pb+Pb.

The difference of the total incident energy of the beam particle between 200 AGeV/c sulphur (6.4 TeV) and 160 AGeV/c lead (33 TeV) is 5.2 as a ratio of those two total energies. On the other hand, the ratio of measured dN/dy Pb+Pb over S+S is 7.2 $\pm$ 0.9, which is larger than the ratio of the two beam energies. dN/dy distributions of negatively charged particle measured at NA35/NA49 experiment for both 200 AGeV/c S+S and 160AGeV/c Pb+Pb at SPS are presented in the figure 5-4. The shape of the distribution does not change too much, the ratio Pb+Pb over S+S is around 8.2 $\pm$ 0.3 [5-2]. The difference of the absolute value of dN/dy between NA44 and NA35/NA49 may be caused by the difference of centrality and the difference of particle identification. Assuming a similar production between pion$^+$ and pion$^-$, the ratio of dN/dy as Pb+Pb over S+S measured in the both experiments are clearly larger than the ratio of these two beam energies. This increase may suggests an increase of the re-scattering during the collisions and a higher baryon stopping in Pb+Pb collisions and some degree of transparency in S+S collisions, which will be discussed in the following section. Those pion rapidity distributions are too broad to be purely thermal. Those data rule out thermal models which incorporate a spherically symmetric radial expansion, but but are consistent with hydro-dynamical models which assume primarily longitudinal expansion.

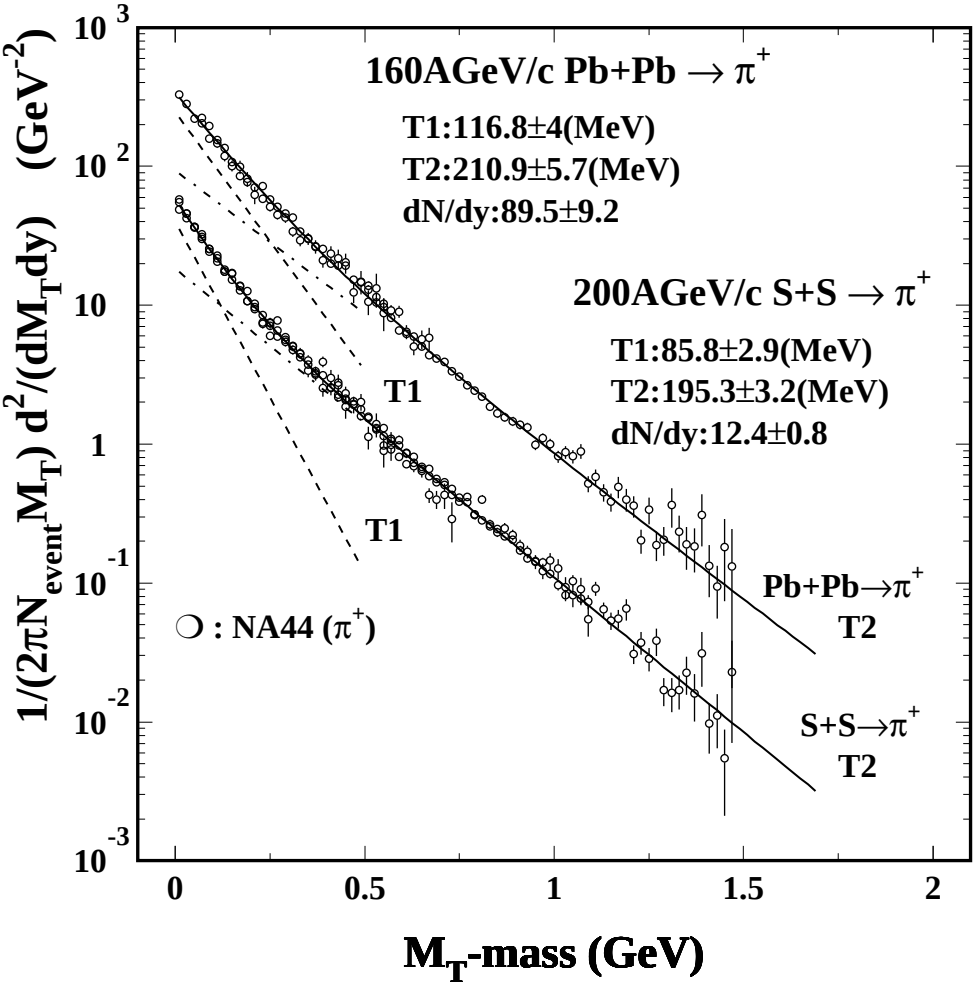

Figure 5-3: normalized invariant cross section for pion

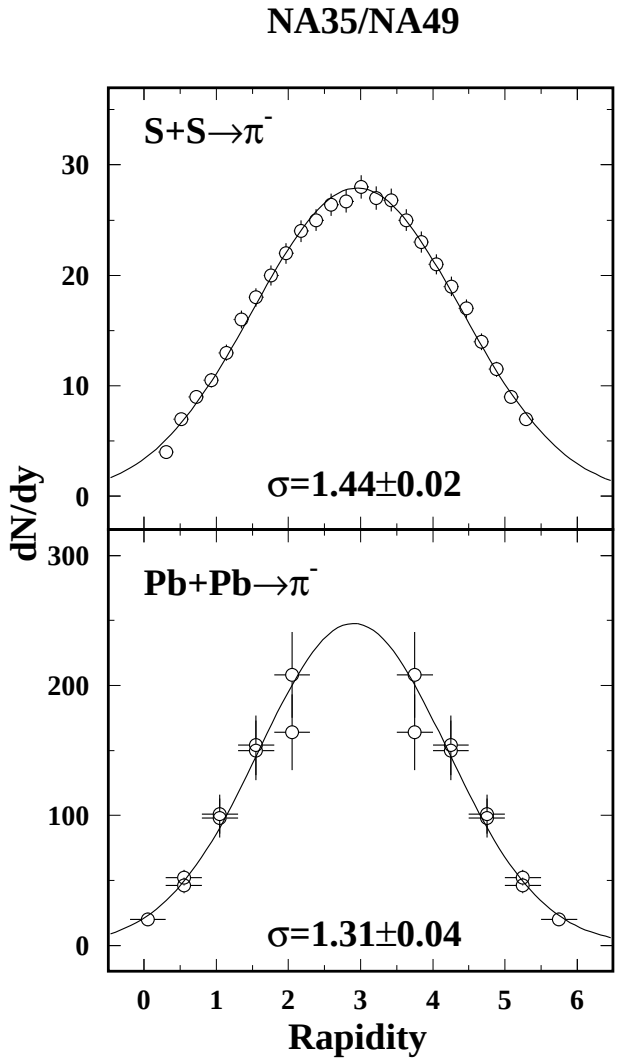

Figure 5-4: pion$^-$ dN/dy

5.3 Proton rapidity distributions

Proton rapidity distributions for sulphur on sulphur collisions and for lead on lead collisions will be presented in this section and shown in the figure 5-5. dN/dy's are calculated by integrating the absolutely normalized transverse momentum spectra with assuming single exponential shape, where this method was described in the previous chapter. These calculations were done at 8GeV/c and 4GeV/c momentum settings at horizontal spectrometer magnet configuration, the different momentum setting with NA44 spectrometer gives the another measurement at the different rapidity (smaller rapidity at the smaller momentum setting). Because of the collision symmetry for both S+S and Pb+Pb, two measured points dN/dy's are reflected around the central rapidity. Proton rapidity distribution is a strongest tool to measure the nuclear stopping power. Because of the baryon number conservation during the collisions, total number of the proton over the full phase space can not excess too much above the original proton number in the colliding two nuclei, since $N\overline{N}$ pair production is not big at this energy. By fixing the integrated number of proton over rapidity to be a constant at the original number of the colliding two nuclei, proton rapidity distribution can be used to measure the amount of the stopped proton at central rapidity in order to estimate the nuclear stopping power.

By comparing the shape of the two rapidity distributions for S+S and Pb+Pb, a flat plateau or U shape distribution around the central rapidity seen in the lighter ion collisions is changed into a center peaked distribution in the truly heavy-ion collisions. The first, a flat plateau rapidity distribution is already telling that the nuclear transparent picture is not completely right at this SPS energy, the nuclear stopping is already increasing in the S+S collisions. This phenomenon of the center peaked rapidity distribution is clearly saying that the higher nuclear stopping in achieved in the Pb+Pb collisions. This proves that the higher baryon density region is exist around the central rapidity.

The high baryon density may cause the large re-scattering between the produced particles, and thermalization of the system may achieved around the central rapidity. The results which has seen on the transverse momentum spectra of the secondary particles in the previous section is confirming this increase of the nuclear stopping power.

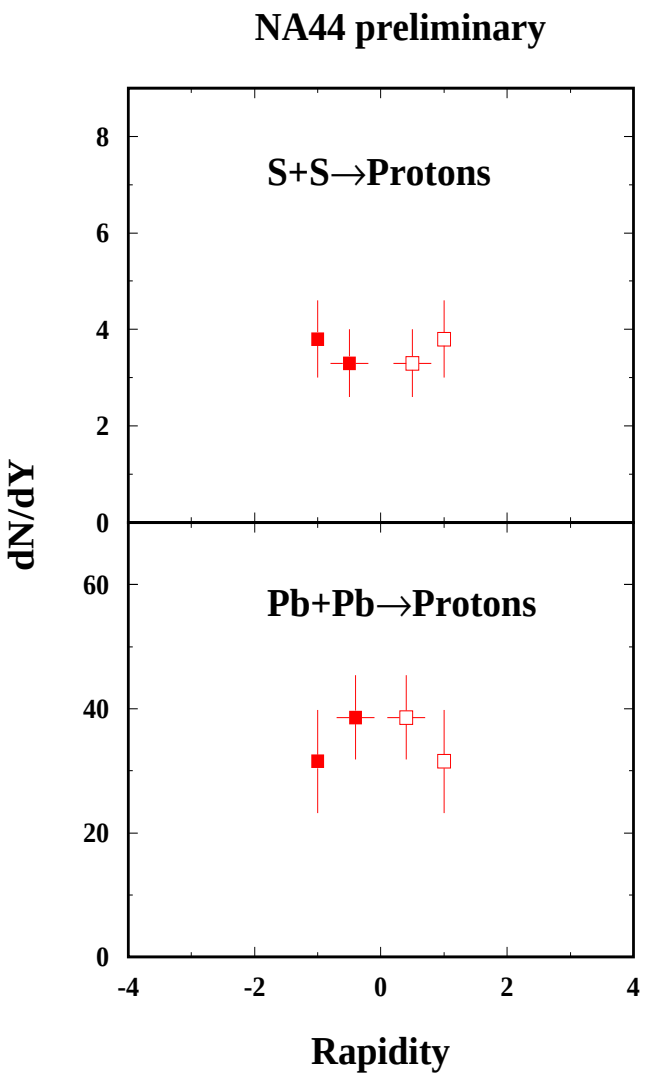

Figure 5-5: proton dN/dy

5.4 Two particle interferometry for pions and kaons

Two particle correlation functions for pions and kaons in sulphur on lead collisions around central rapidity are presented in this section. Two pion event samples are collected at two different transverse momentum regions, low P_T region ($0.0 < P_T < 0.4$) and high P_T region ($0.3 < P_T < 0.8$), which are corresponding to two different spectrometer angle settings, small angle setting (44 mrad) and large angle setting (131 mrad), they are taken both at the 4GeV/c spectrometer momentum setting. On the other hand, two kaon event samples are collected at the 6GeV/c small angle setting, covered transverse momentum range is ($0.0 < P_T < 0.6$). Data presented here are analyzed in two dimensionally in (Q_T,Q_L) in order to focus on the transverse size R_T of the emitting source of the identified particle. Because the data are taken at horizontal magnetic setting, transverse momentum difference Q_T is domained by Q_{TO}. Therefore the measured R_T is mainly influenced by R_{TO}, which is a combination of the transverse size and the time duration of the particle emitting source distribution.

Two dimensional chi-square contour maps are shown at the fixed λ having the lowest chi-square for each setting in the top three figures in the figure 5-6. Here the procedure to make these chi-square contour maps are explained in the previous chapter. Experimental correlation functions and Monte Carlo output correlation functions which have the smallest chi-square are shown on the top of each other for the comparison in the figure 5-6. Fully corrected two dimensional correlation functions in Q_T and Q_L and those projections can be seen in the next figure 5-7.

The similar transverse size R_T around 2-3 (fm) for both high P_T pions and low P_T kaons are observed, compared with the larger transverse size around 4 (fm) for low P_T pion. The larger size of low P_T pion can be explained by the resonances contribution ω, η and η' or other heavy resonances having a long life time. At higher P_T, those contribution to pion are estimated to be smaller than at lower P_T. Charged kaon are less affected by resonance decay than pions. The result is that pion and kaon source sizes in the resonance-less region are found to be comparable. This suggests pions and kaons are emitted from similar space region and time duration of the colliding system, which is consistent with the previously mentioned scenario that all hadrons are frozen-out at the same freeze-out temperature with the same velocity. This results add one more confidence to the freeze-out scenario, which is the same freeze-out volume for all hadrons.

On the other hand, there is another explanation to the resulting source sizes. A simple hydro-dynamical model, which predict the radius parameters to scale as $1/\sqrt{M_T}$ for all mesons. The collective expansion will create a strong position-momentum correlation in both longitudinal and transverse directions. The velocity gradient together with the freeze-out temperature generate a length scale in all three dimensions. If the source length scales are considerably larger than this, for a cylindrically symmetric three dimensional expansion, the measured radius parameters become equal in the LCMS system and will show $1/\sqrt{M_T}$ dependence [2-2]. In

the figure 5-8, the measured data are complied as a function of M_T, the solid line shows the fitted line with $A/\sqrt{M_T}$, where A is a fitting parameter. The data agree with this hydro-dynamical model fairly well, too. If this is right, the measured sizes are not representing the real source size, it's just kinematical effect which is coming from the position-momentum correlation caused by the radial and longitudinal expansion, however the $1/\sqrt{M_T}$ dependence also depends on the strength of the position-momentum correlation compared to the source extension.

One more consideration to the measured source size is the experimental acceptance. Because of the narrow momentum acceptance of the experiment and the position-momentum correlation of the expanding source, the experimental acceptance will directly define the size of the window or the aperture of our telescope, which is a tool called a two particle interferometry in this case. This means that two particle event samples are collected from the small fraction of the total particle-emitting source distribution, in another word, our telescope looks only small part of whole fire ball. In addition to this, the position-momentum correlation will reduce the measured source size even more, if one measures the source size with two particle interferometry technique. The reason is exist inside of the interferometry technique itself, an enhancement of detecting two identical particles which have two close momenta, in another word, which come from two close positions caused by the strong position-momentum correlation, will define the measured source size. In this sense, the interferometry technique is in principle not suitable to measure the size of the expanding source, which has the strong position-momentum correlation, since it is not chaotic source. To understand the expanding source and the interferometry, one needs to distinguish contributions into the measured source size from the geometrical size and the size made by the position-momentum correlation. Therefore, it is important to compare the measured data with model simulations. This will be discussed in the following chapter.

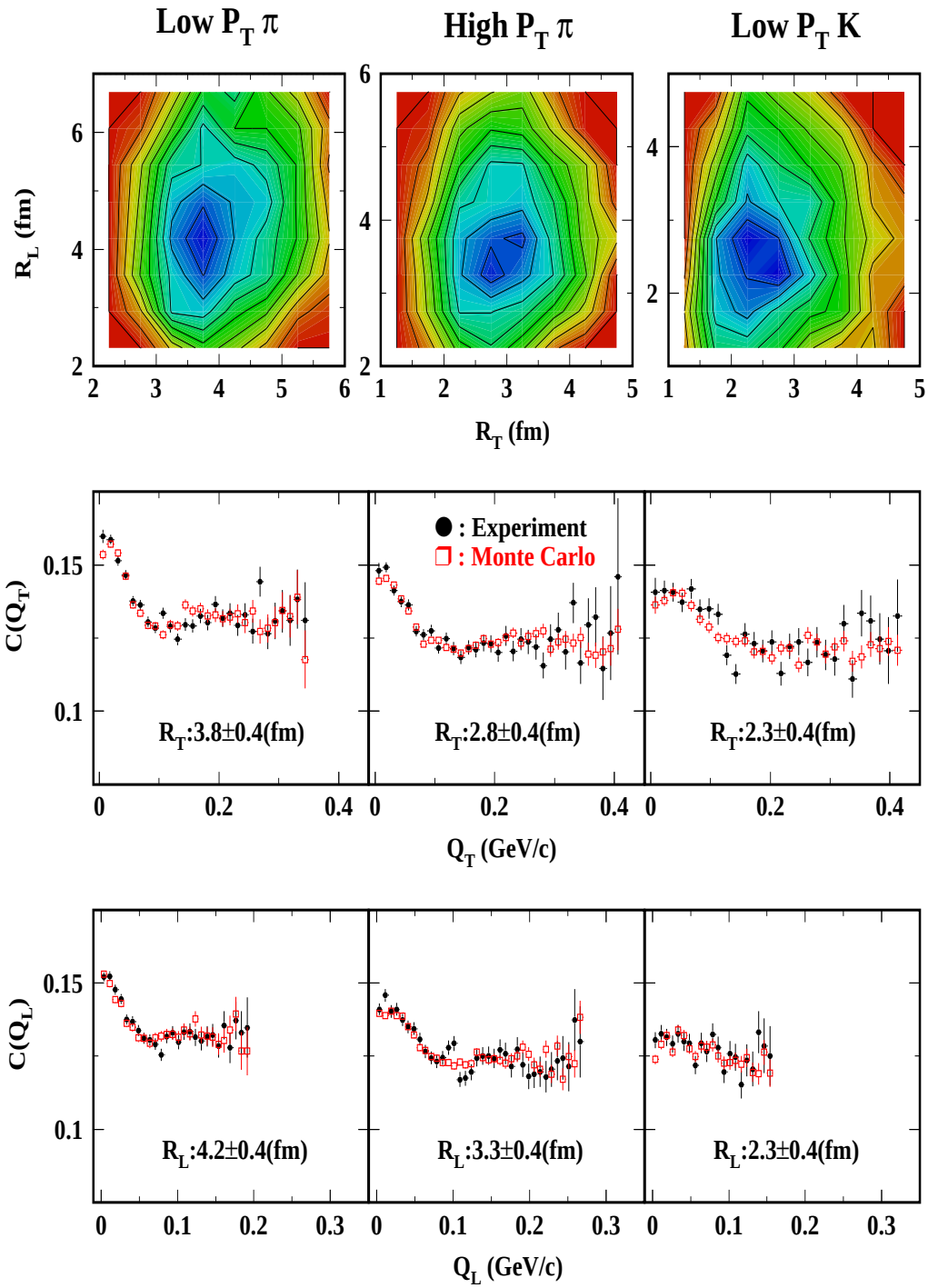

Figure 5-6: chi-square map and comparison with MC at the smallest chi-square

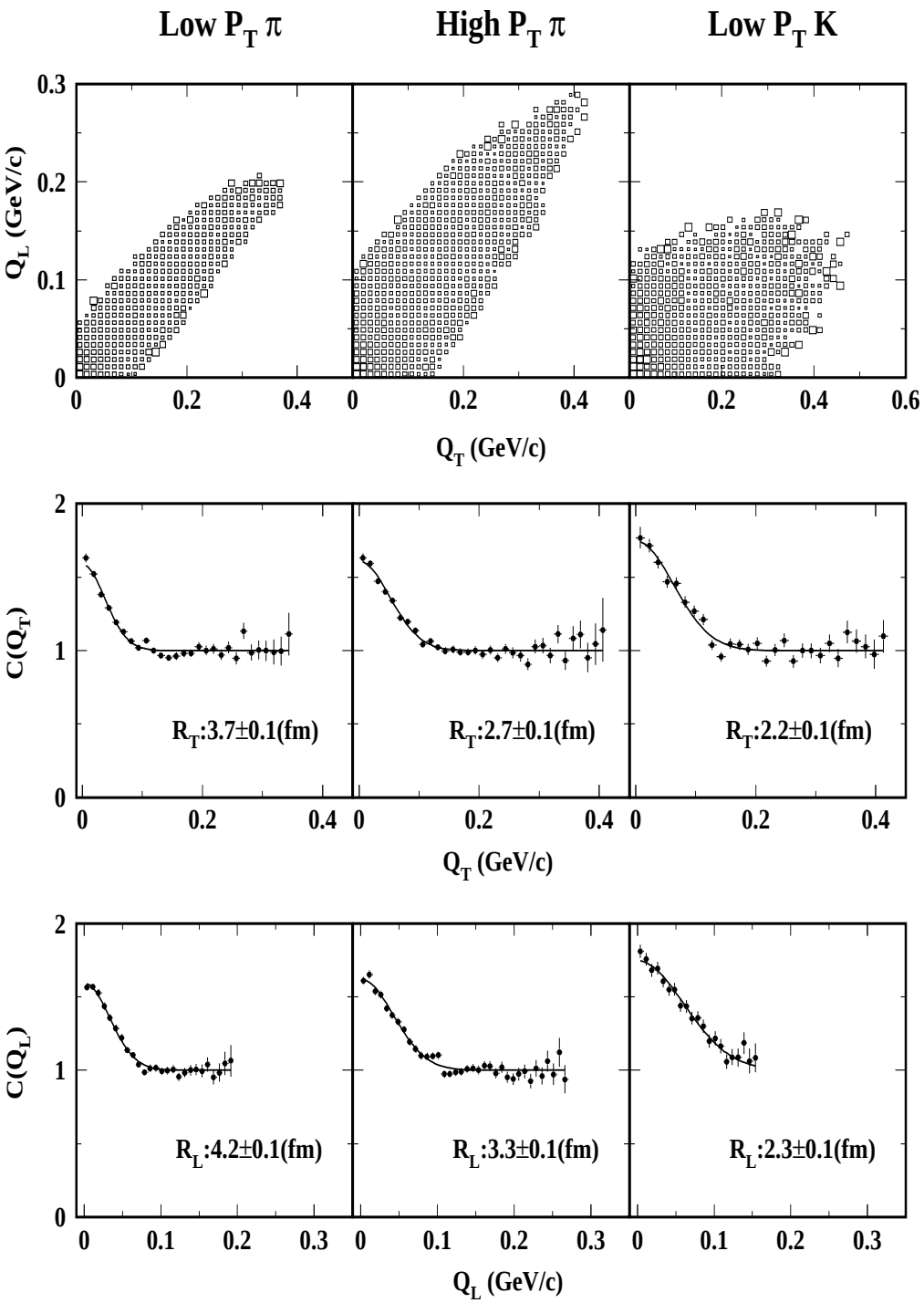

Figure 5-7: corrected two-dimensional correlation functions and projections

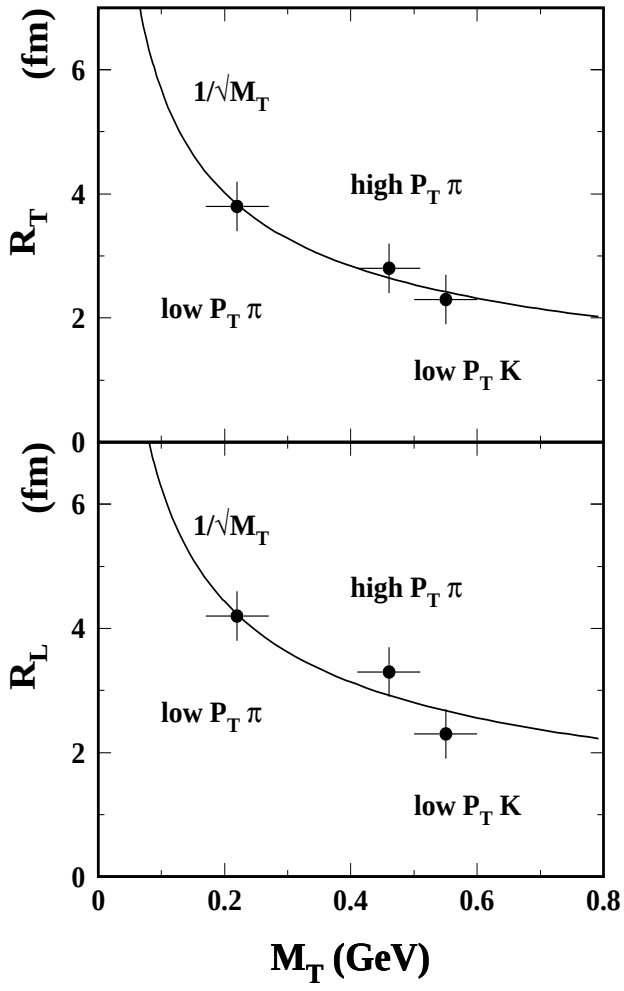

Figure 5-8: summary of measured radius parameters

Chapter 6. Model comparison

6.1 comparison with RQMD

Data shown in the previous chapter are compared with a microscopic cascade model 'relativistic quantum molecular dynamics' (RQMD). The characteristics of the RQMD model will be pointed. (1) The interaction probabilities are given by geometry. (2) The dominant production mechanism in the first stage of the collision is the excitation of both collision partners to resonances or strings. (3) Excitation of baryons can also be come from the secondary interactions, which are dominated by annihilation of produced mesons on baryons. (4) Those formed resonances contribute to strangeness enrichment and are further excited by subsequent collisions to create $N\overline{N}$. (5) The formation time of newly produced secondaries is given by the finite life time of a resonance or by the time which a string needs to break into parts which is given by the momenta of the fragments. (6) Such multistep process is viewed as a complicated interplay between excitation and decay processes. (7) The fate of all particles including newly produced ones as well as the original ones is followed by propagating those particles on classical trajectories and allowing collisions between all of them until the cascade process is finished.

Transverse mass spectra for three particle species for both colliding systems are compared with the RQMD model, too. The figure 6-1 shown here is the same one in the previous chapter, and RQMD spectra are overlapped for each slopes. The invariant cross sections $1/M_T\ dN/dM_T$ are arbitrary normalized for each spectra. The transverse mass spectra calculated by the RQMD model agree with the inverse slopes for pions, kaons and protons for both sulphur on sulphur collision system and lead on lead collision seen in the experimental data, except low P_T pions for both systems and low P_T protons for Pb+Pb collisions. Global trends of the slopes for those three particles are reproduced by the microscopic cascade RQMD model. This suggests that the transverse flow effect which has been described in the previous chapter might be created by superimposing of binary N+N collisions and re-scattering cascade during the collisions.

Comparison of measured transverse mass spectra by NA44 and NA35 and one from RQMD simulation for pion for S+S and Pb+Pb collisions is shown in the figure 6-2, where one can see clear deviation between experimental measurement and RQMD simulation at low P_T region. Heavy or long lived resonances contributions to the pion M_T spectra from RQMD simulation are shown in the figure 6-3. Those resonances contributions are clearly seen at lower P_T region and make the steep component, which corresponds to the small inverse slope parameter, in the invariant M_T distribution. Low P_T enhancement can be explained with those contributions qualitatively, but quantitatively the low P_T enhancement is not enough in the RQMD simulation, although the data from both NA44 and NA35 experiment [5-2] show more remarkable enhancement, which can be found in the figure 6-2. The heavy or long lived resonances contributions have also studied for the emission position

distribution of the secondary hadrons as seen in the figure 6-4. Those resonances contributions are found to be wider than the others seen in the figure, because of the longer life time. Combining two pictures of transverse mass spectra and emission position distributions with or without the resonances contributions, those resonances will affect the pion transverse mass spectrum at lower P_T region, which will cause the low P_T enhancement, and the large pion source size at low P_T region. This tendencies are consistent with the experimental measurements, qualitatively.

Proton rapidity distribution are compared between RQMD model and data measured at NA44 experiment shown in the figure 6-5. Similar centrality selection to RQMD events is done to compare it with the experimental data. For comparison, RQMD calculation for proton on proton collision is added on the top of the figure in order to compare with sulphur on sulphur collisions and lead on lead collisions. Integrated number of the proton rapidity distribution should be conserved to almost the number of the original colliding two nuclei as mentioned in the previous chapter. The fraction of the number of the stopped protons at the central rapidity region is clearly increasing with the size of the colliding system. Higher degree of the nuclear stopping power is also seen in the RQMD model at truly heavy-ion collisions. The value and shape of dN/dy of RQMD model reproduce the experimental data fairly well. Rapidity shifts, which correspond to a direct measurement of the nuclear stopping power, are calculated as an average rapidity over the forward rapidity region except the spectator peak at the rapidity wing, by using the dN/dy distribution of RQMD simulation. Those numbers are seen in the figures, and are the highest almost around 2 units of rapidity at the heaviest lead on lead collisions. This also proves the higher stopping power at the heaviest system at SPS energy.

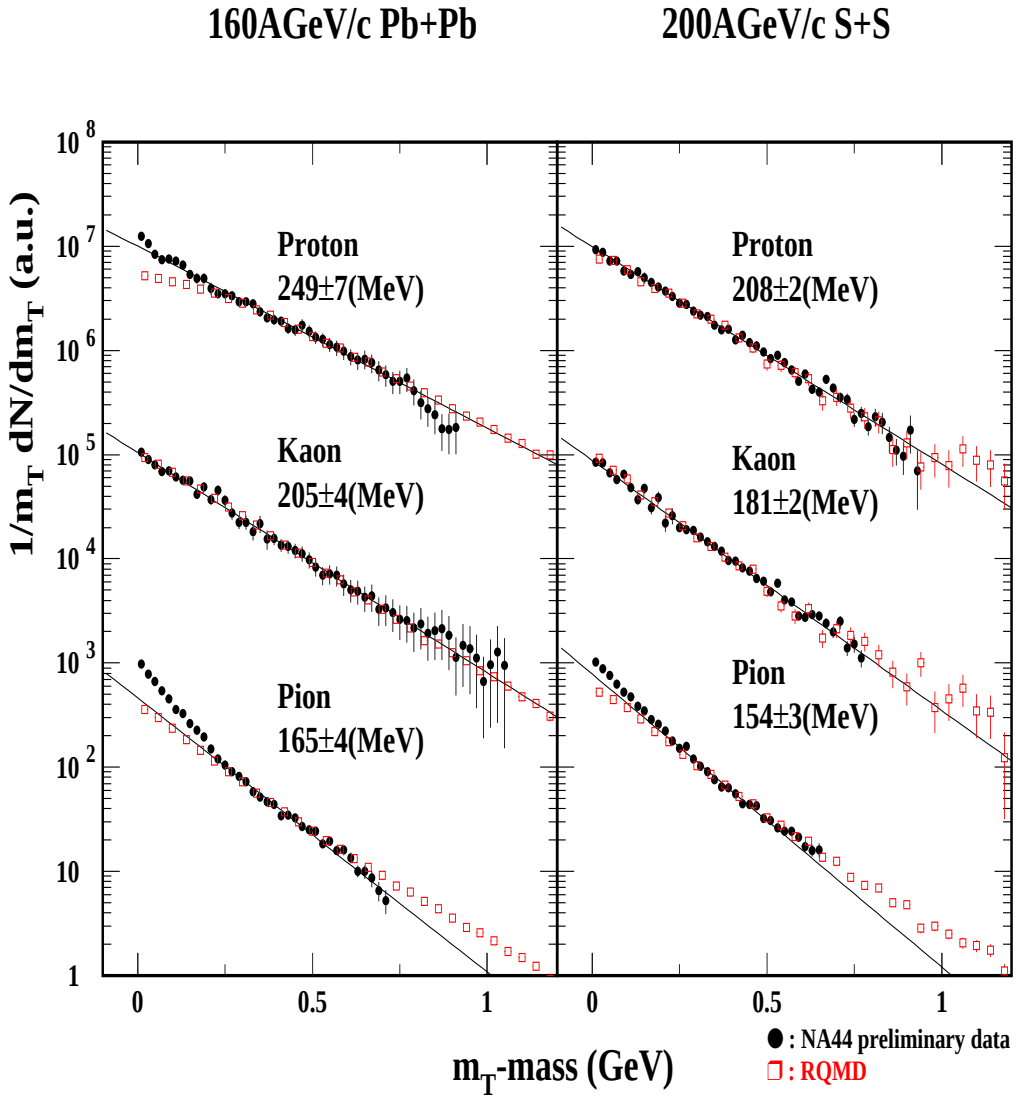

Figure 6-1: transverse mass spectra

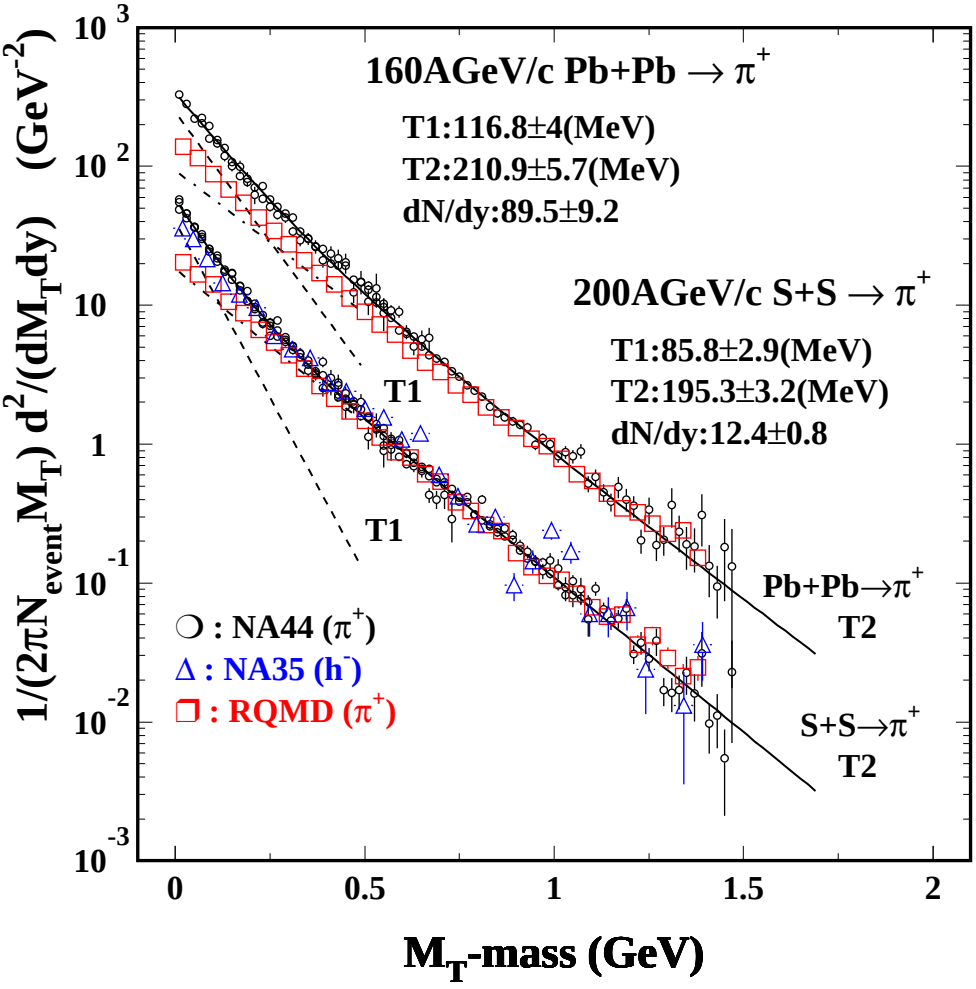

Figure 6-2: comparison of inverse slopes for pion

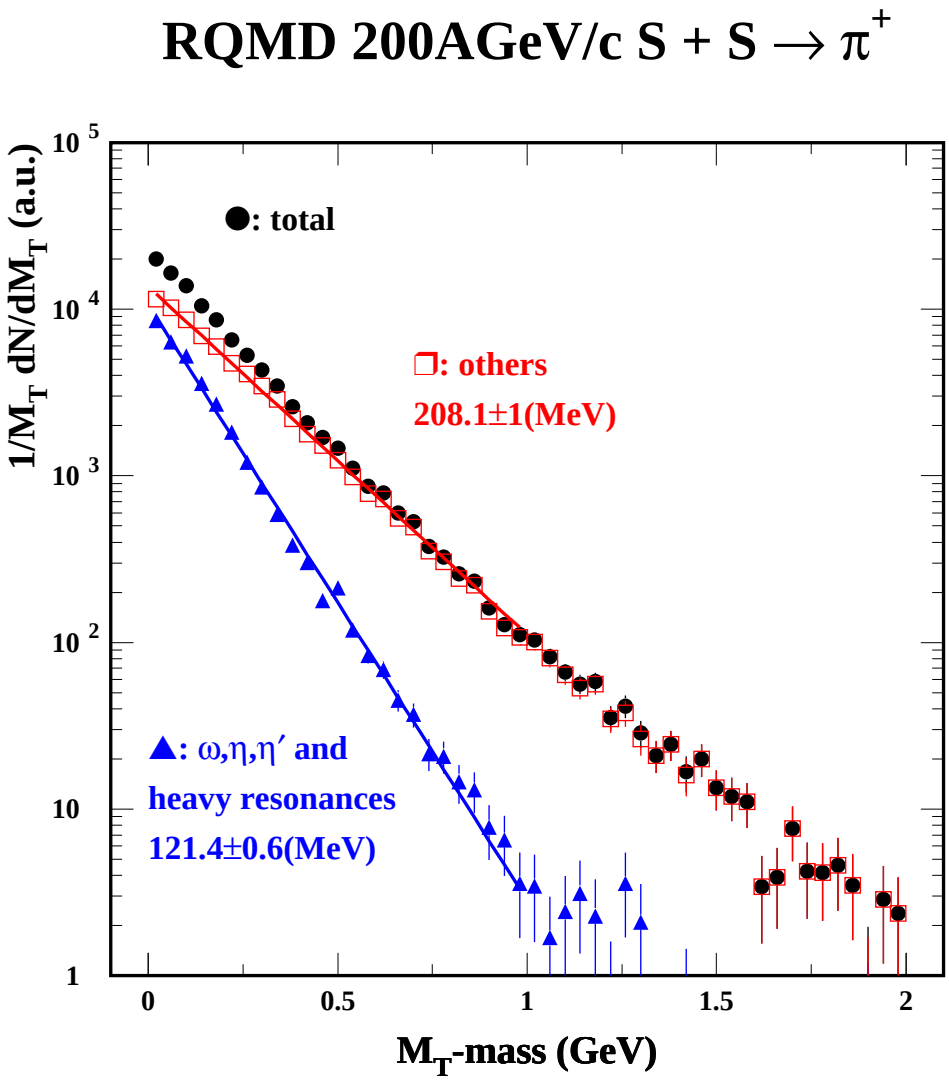

Figure 6-3: heavy resonance contribution to inverse slope

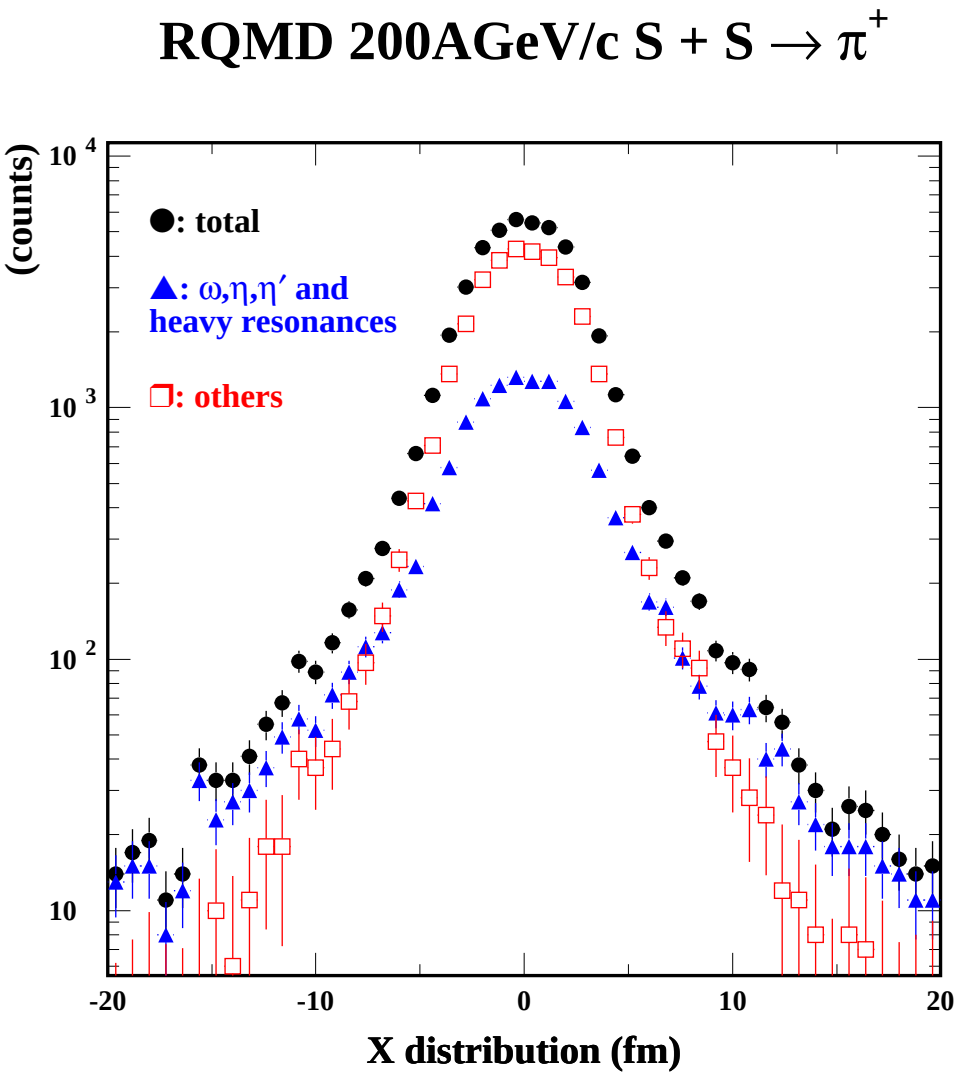

Figure 6-4: heavy resonance contribution to source distribution

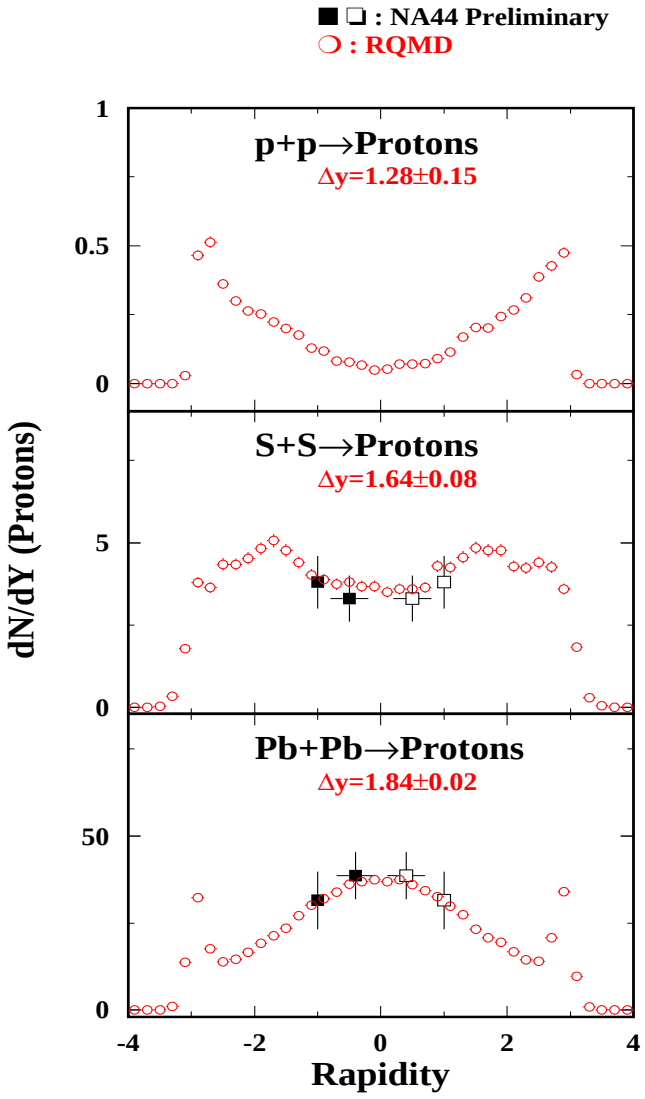

Figure 6-5: proton dN/dy distributions

Pion source distributions from the RQMD simulation are made for each slices of P_T range shown in the figure 6-6. As one can see that the width of the whole distribution does not change with increasing the P_T too much. However, inspecting the center-top shape of each distribution, rather flat bell shape distribution at lower P_T region is changed to volcanic U shape distribution, which will make the doughnut shape in X-Y plane, at higher P_T. This change is caused by the previous mentioned position-momentum correlation of the expanding source. Superimposed histograms are accepted-particle source distributions by the NA44 spectrometer at 4GeV/c small angle, 4GeV/c large angle and 8GeV/c large angle settings. The accepted-particle distribution changes its own peak position toward the negative X direction and the width of the distribution decreases with increasing the P_T, this is purely kinematical effect, that is the position-momentum correlation and the experimental acceptance. X distributions requiring the acceptance are always shifted toward negative in X direction, the reason of this is that (1) the NA44 spectrometer is sitting at the negative X side respecting to the beam line, and (2) therefore the experimental momentum acceptance covers mainly negative P_X ($-0.4 < P_X < 0.05$ GeV/c for 4GeV/c small angle setting, $-0.8 < P_X < -0.2$ GeV/c for 4GeV/c large angle setting and $-0.6 < P_X < 0.05$ GeV/c for 6GeV/c small angle setting), although P_Y acceptance is symmetry and small ($\pm$ 0.05 GeV/c), and (3) strong position-momentum correlation of expanding source distribution, which is demonstrated with the RQMD simulation in the figure 6-7. Experimental acceptance itself has a tendency to reduce the size of particle emitting source distribution with increasing P_T. The figure 6-8 summarizes the width of the pion source distribution with and without requiring the experimental acceptance as a function of M_T.

Source distributions of pion and kaon given by the RQMD simulation are shown in the figure 6-9. Top two figures show the pion source distributions in X and Y directions, where both directions are perpendicular to the beam direction, bottom two figures are same for kaon source distributions. Kaon source is found to be smaller than pion without requiring experimental acceptance. Several reasons can be listed, kaons are less affected by resonance decay than pions, the smaller cross section of kaon with nuclear matter compared to pion may cause the different (earlier) decoupling time from the particle emitting source. Superimposed histograms in the same figure show the same source distributions with requiring the acceptance for pion at 4GeV/c small angle setting corresponding to low P_T region and at 4GeV/c large angle setting corresponding to high P_T region, and for kaon at 6GeV/c small angle setting. The next figure 6-10 also shows the emission source distributions (X, Y, Z, and time) in the LCMS frame, where total P_Z of two particles is zero, which can be defined only with two particle events in the experimental acceptance. The fitted sigma parameter with Gaussian function are shown in the figures for each distribution. A trend of experimentally measured radius parameters for various settings with the interferometry technique are reproduced qualitatively in the RQMD emission source distributions. This may suggest that the source length scale of particle emitting source distribution with requiring the NA44 experimental acceptance is smaller than the length scale created by the position-momentum correlation from

the expansion.

By using RQMD source distribution cooperated with SPACER program, correlation functions are created to compare the shape of the correlation functions and to compare measured source size by fitting the correlation function with the experimental data. The spacer program calculates a correlation function for given single particle phase-space distribution by symmetrizing the wave function, therefore in this way, the fitted source size parameter will be affected by the position-momentum correlation generated in the RQMD simulation. Created correlation functions are compared with experimental correlation functions for each setting, the comparison is shown in the figure 6-11. Correlation functions without resonance, (no ω, η, η' for pion), (no ϕ, K^* for kaon) are superimposed on those figures in order to see the effect of the resonances. Those resonances contribute to make the λ parameter smaller, where the λ shows an amplitude of the correlation and is intersection of the correlation function, and to make the width of the enhancement smaller, which means that it makes the radius parameter larger. Those effects are found to be larger at low P_T as seen in the single particle spectrum. Fitted radius parameters from this calculation have a similar trend found in the experimental data, although the λ parameters of the calculation are larger than that of experimental data for all cases. This also tells that the resonances contribution in RQMD simulation is not enough compared with the experimental data. The source distribution and the correlation function of pion at 8GeV/c large angle setting are also calculated with the simulation, although there is no experimental data. The width of the fitted source distribution ($\sigma_{\rm dist}$) from RQMD simulation and the fitted source size of the correlation function created by RQMD simulation and SPACER program are shown to compare with the measured source size in the figure 6-12. The simulation shows a clear deviation in R_T from the fitted function $1/\sqrt{M_T}$ to the experimental data. The experimental data measured at 8GeV/c large angle setting will give clear and unique solution.

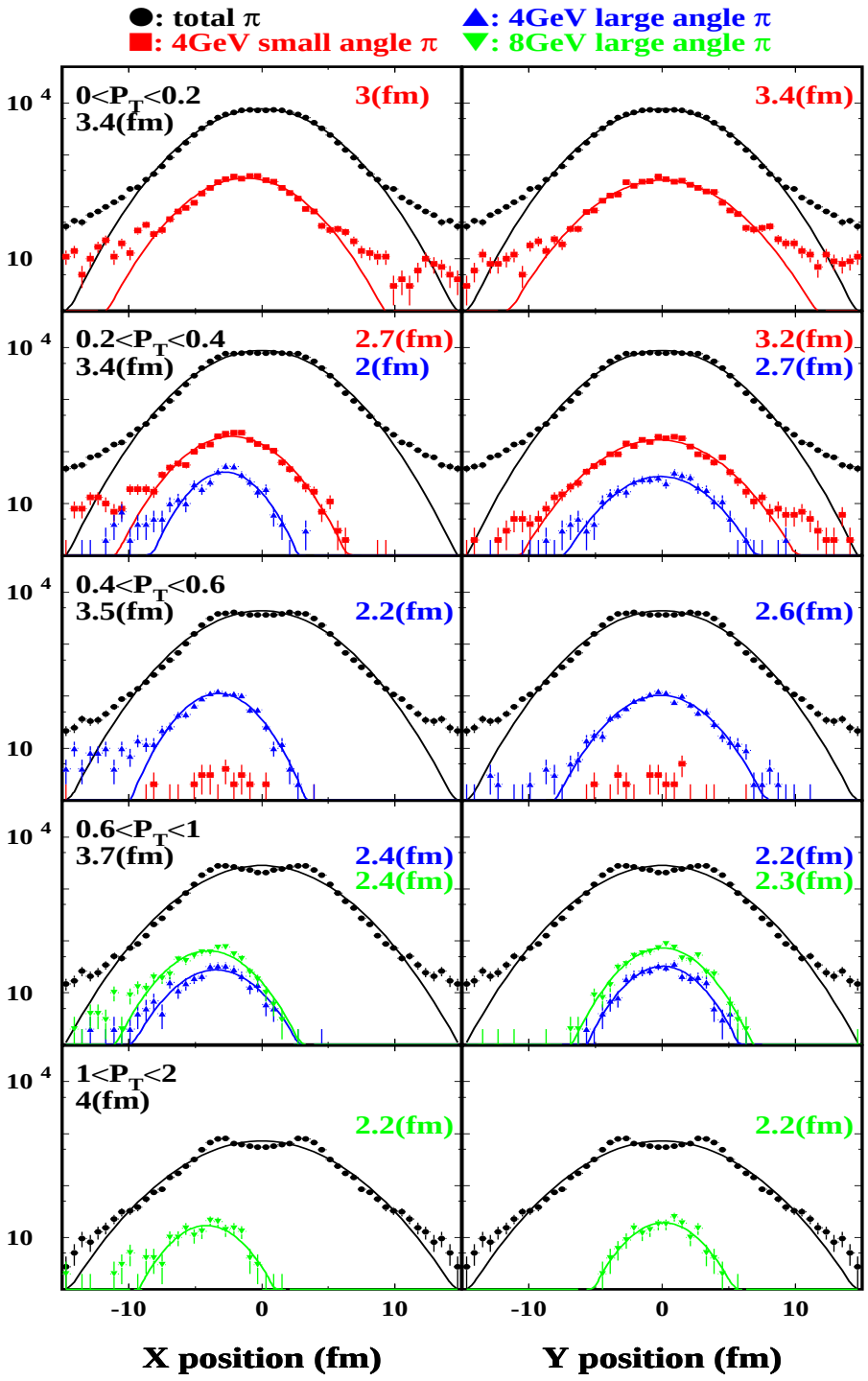

Figure 6-6: P_T dependence of the pion source distribution

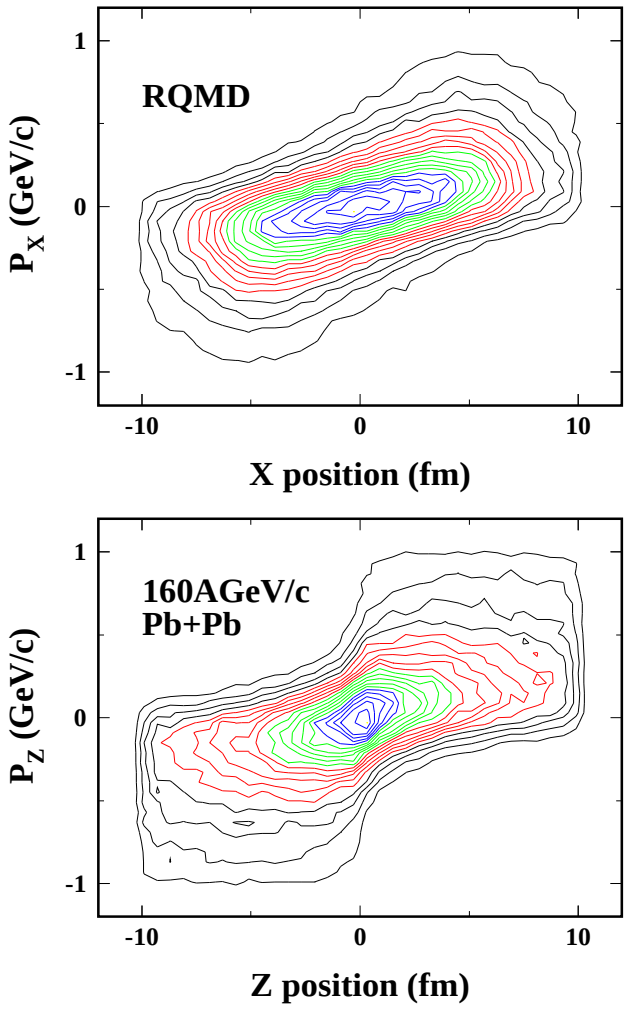

Figure 6-7: position-momentum correlation generated in RQMD

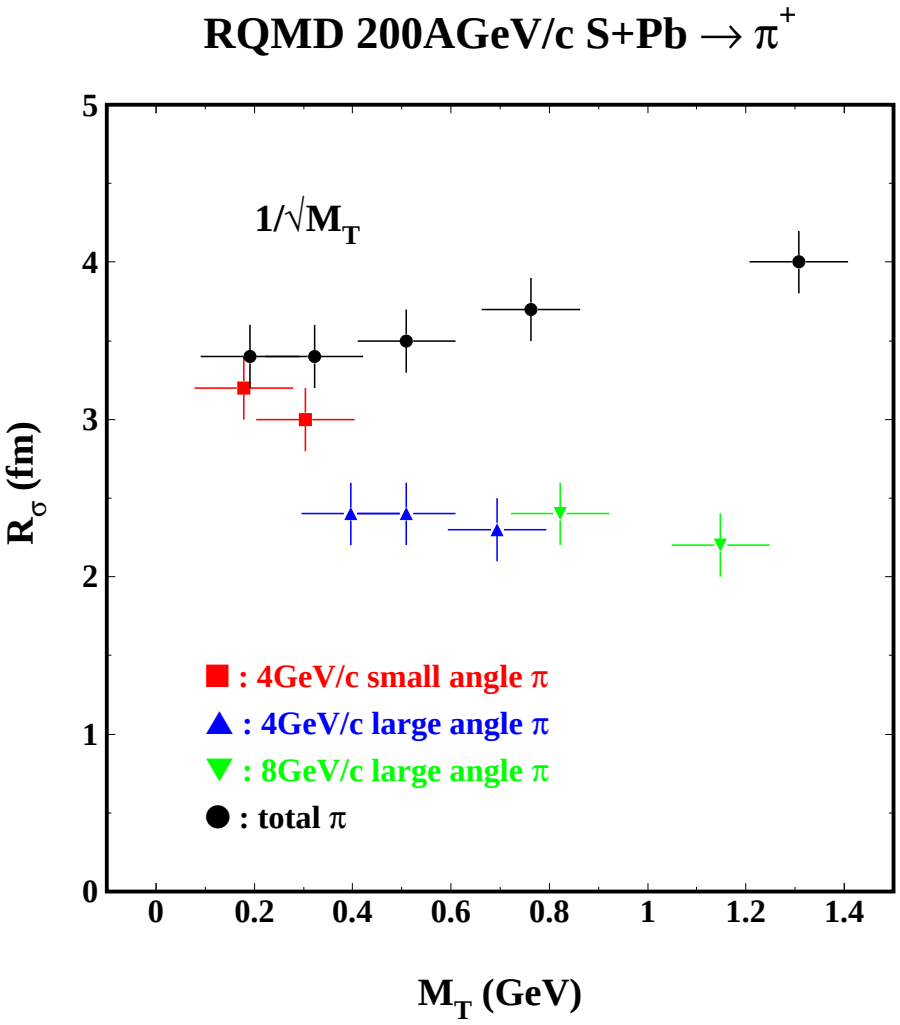

Figure 6-8: summary of the width of the pion source distribution

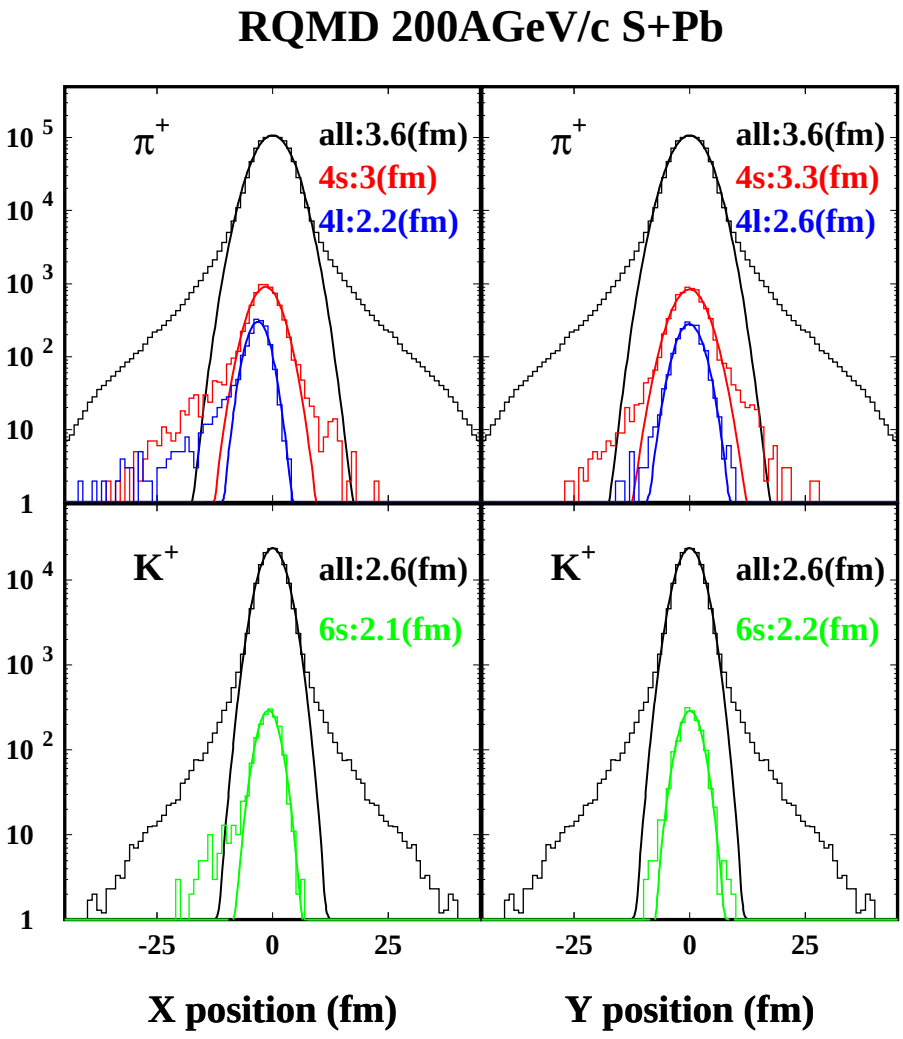

Figure 6-9: source distributions for pion and kaon

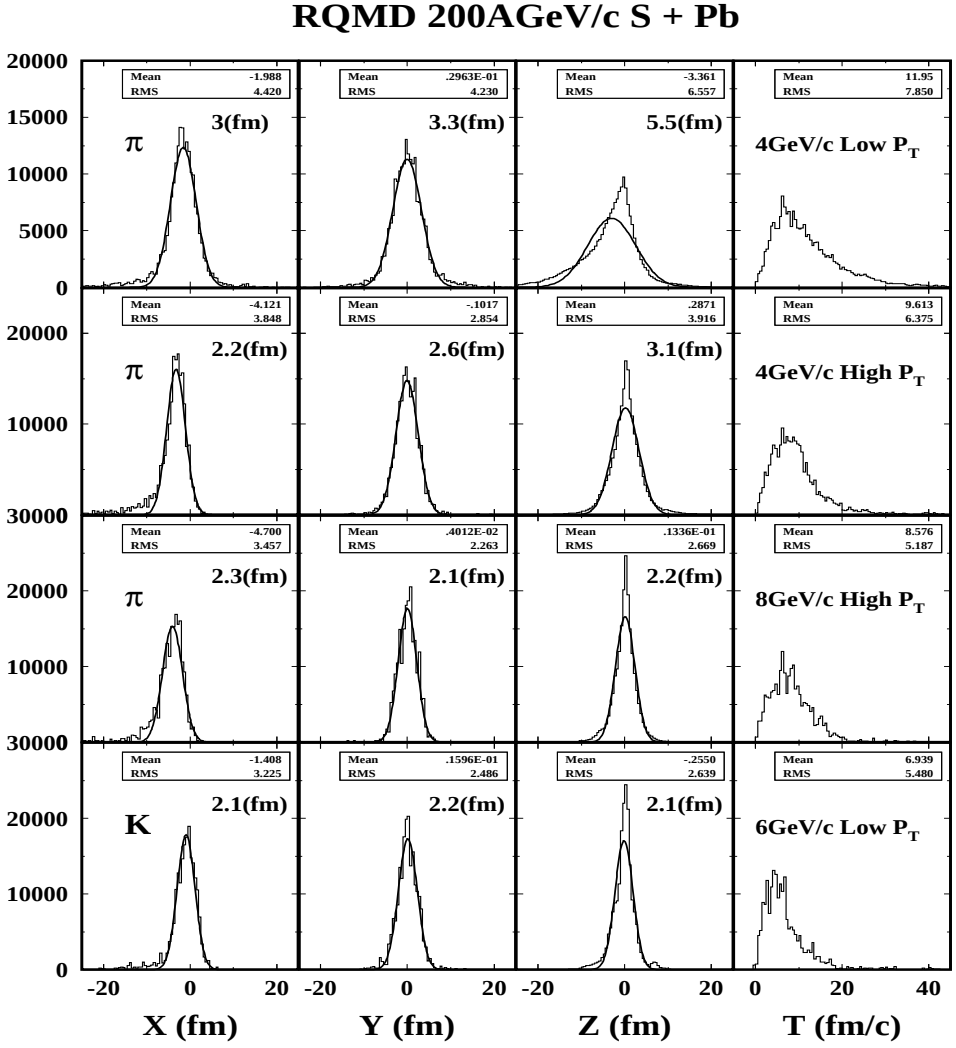

Figure 6-10: source distributions for several settings

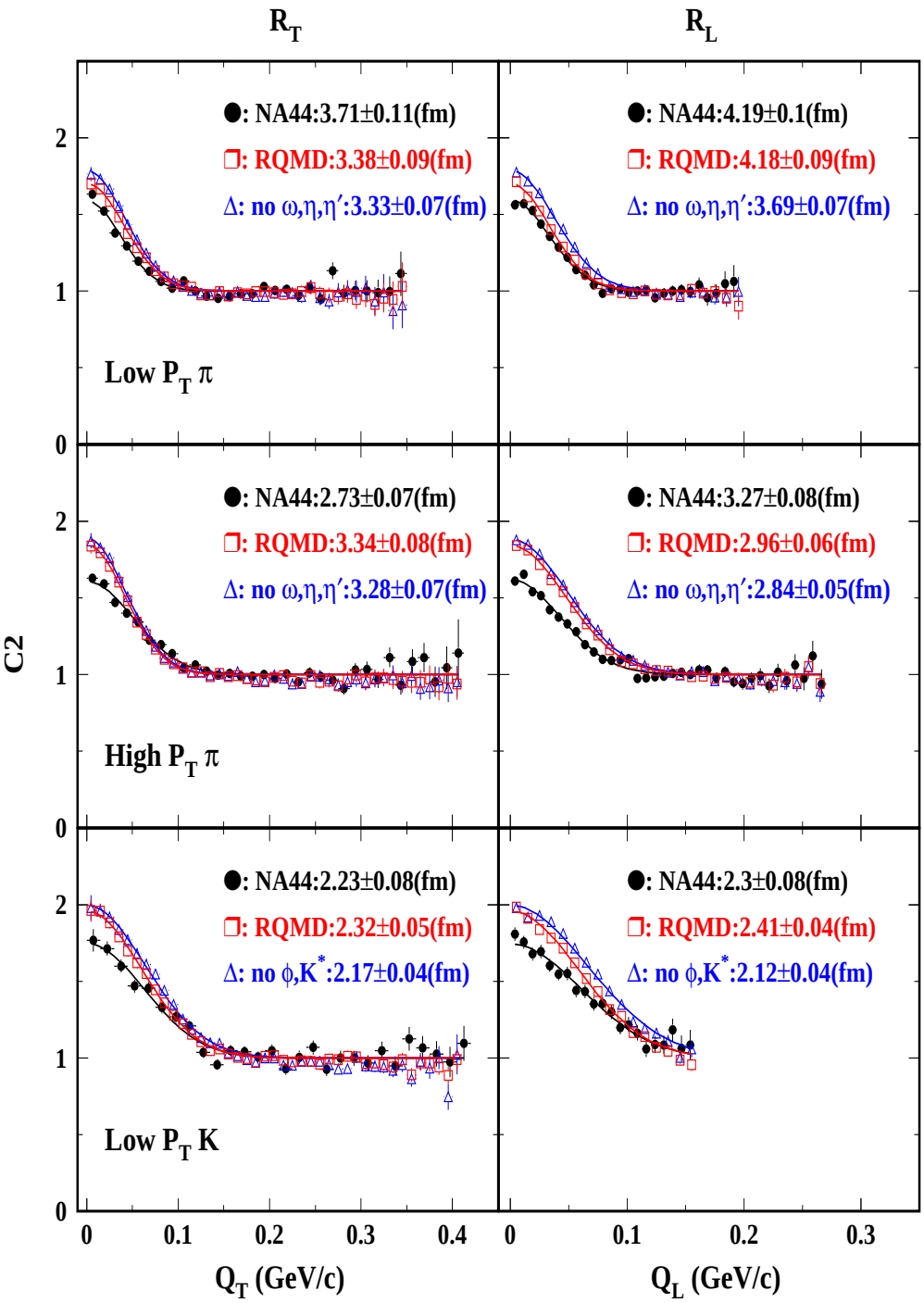

Figure 6-11: comparison of correlation functions

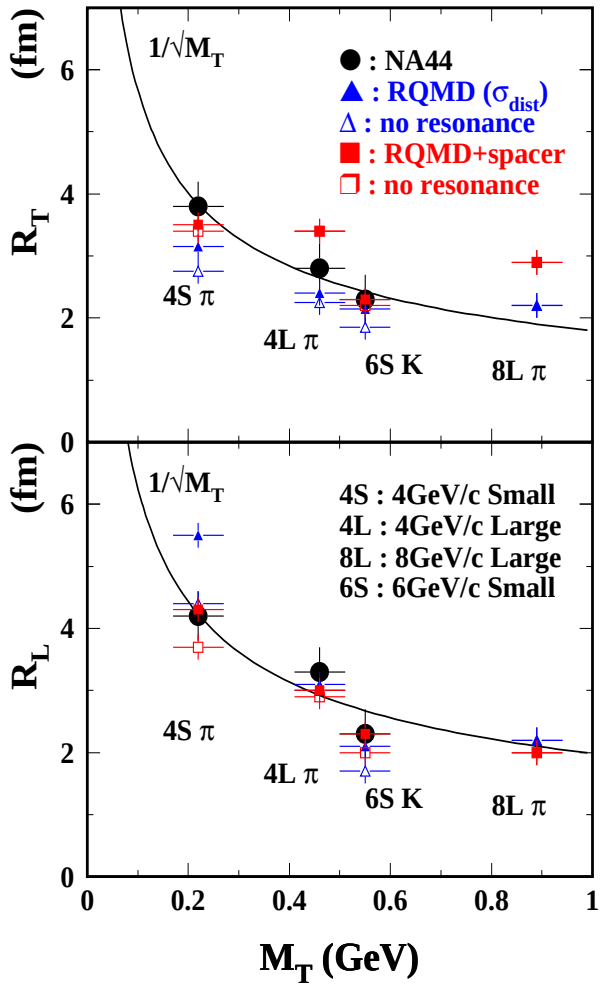

Figure 6-12: summary of the source size

6.2 comparison with hydro-dynamical model calculation

The transverse mass spectra are compared with a hydro-dynamical model calculation. The formula of transverse mass spectrum from the hydro-dynamical model calculation can be found in the reference and is described in the following formula.

$$\frac{1}{M_T}\frac{dN}{dM_T} \propto \int_0^R r dr M_T I_0(\frac{P_T sinh\rho}{T_f}) K_1(\frac{M_T cosh\rho}{T_f}),$$

where the spectrum is a superposition of the individual thermal components, which are boosted with the boost angle $\rho = tanh^{-1}\beta(r)$. $\beta(r)$ is a transverse velocity distribution, which is defined as $\beta(r) = \beta_s(r/R)^\alpha$ in the region of $(0 < r < R)$, where a power of α will change the form of the velocity profile. In the following calculation, $\alpha = 1$ is used. I_0 and K_1 are well known as modified bessel functions. This formula is therefore parameterized by a freeze-out temperature (T_f), a surface velocity (β_s) and a mass of the particle [6-2,3].

Now, this transverse mass spectrum given by the formula is used to describe the experimentally measured spectrums shown in the previous chapter. Three experimentally measured slopes of pions, kaons and protons for each colliding system will be tried to be reproduced by the hydro-dynamical calculation with single T_f and β_s, in order to examine a scenario that an expanding fire ball of the colliding system will be frozen-out (hadronized) at a constant freeze-out temperature T_f for all hadrons with a maximum surface velocity β_s. By fitting those three slopes at a same time, the resulting fitted parameters of T_f and β_s will be given for both S+S and Pb+Pb colliding systems, this will give us some informations for understanding the difference of the expansion or freeze-out feature between the two colliding systems. One set of parameters T_f and β_s successively reproduces the invariant cross sections of pions, kaons and protons as a function of $M_T - mass$ for both sulphur on sulphur collisions and lead on lead collisions, as seen in the figure 6-13, the calculated points are shown in open squares for each slopes. In this calculation, the same freeze-out temperature ($T_f = 140$ MeV) for both colliding systems as a pion mass and is also Hagedorn limit and the different surface velocity ($\beta_s = 0.4$ for S+S and $\beta_s = 0.5$ for Pb+Pb) are used. The figures 6-14 and 6-15 show the comparison between this hydro-dynamical model and the experimental data at the different freeze-out temperature, $T_f = 120$ MeV and $T_f = 100$ MeV, respectively. The model calculations reproduce the measured M_T spectra fairly well for each case.

After making the three slopes for pion, kaon and proton with the above explained formula using the different mass for each particle by fixing the T_f and β_s, one normalization parameter will be fitted for each particle to minimize the fitted chi-square value. Then the total chi-square will be added for those three slopes with the fixed T_f and β_s. This total chi-square will be calculated over and over again in every steps of the T_f and β_s in order to make chi-square map over the two dimensional parameter space of the T_f and β_s. This calculations are done for both colliding systems separately, chi-square contour maps for both systems are shown in the figure

6-16. By looking at the each chi-square map, the resulting parameters T_f and β_s are seen to be not unique, minimum chi-square region has strong correlation between T_f and β_s around (100 MeV $< T_f <$ 140 MeV for both cases, $0.4 < \beta_s < 0.6$ for S+S and $0.5 < \beta_s < 0.7$ for Pb+Pb). However, at any fixed freeze-out temperature T_f, an increase of the surface velocity β_s from lighter to heavier system is clearly seen from those two chi-square contour maps. This also suggests an increase of the transverse flow in truly heavy-ion collision at SPS energy compared to the lighter heavy-ion systems.

Velocity profile dependence of the chi-square contour map is studied by changing the power of α to be 0.5, 1.0 and 2.0. To compare the shape effect with the velocity profile from $\beta(r) = \beta_s(r/R)^\alpha$, the velocity profile from RQMD simulation is extracted by fitting the RQMD profile distribution with the following sigmoid function.

$$\beta(r) = \frac{\beta_s}{exp\{-B\ (r - A)\} + 1},$$

where A and B are the fitting parameters to the profile distribution. Comparison of the velocity profiles is shown in the figure 6-17. By using the four different profiles α = 0.5, 1.0, 2.0 and RQMD type, chi-square contour maps are created over 2-dimensional space T_f and β_s for each velocity profile and for each colliding system. Figure 6-18 shows the chi-square contour maps for different velocity profiles. The resulting T_f and β_s having a minimum chi-square are found to be sensitive to the velocity profile and RQMD profile is somehow similar to α=0.5 velocity profile. α parameter seems to be correlated with β_s, although it does not affect to T_f too much, which might remind one of the roll of the constant C in the formula $T_m = T_f + C\beta_s^2 M$ shown in the previous chapter.

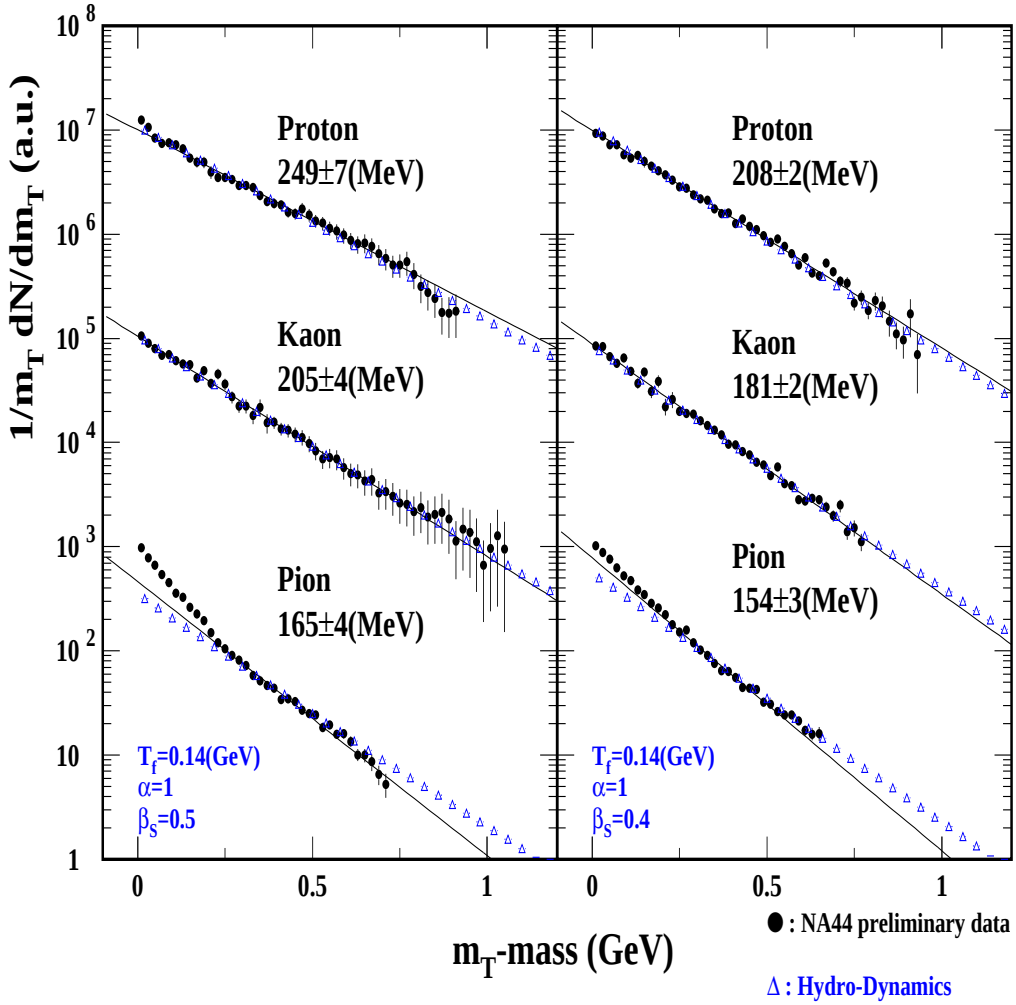

Figure 6-13: transverse mass spectra at T_f=140 MeV

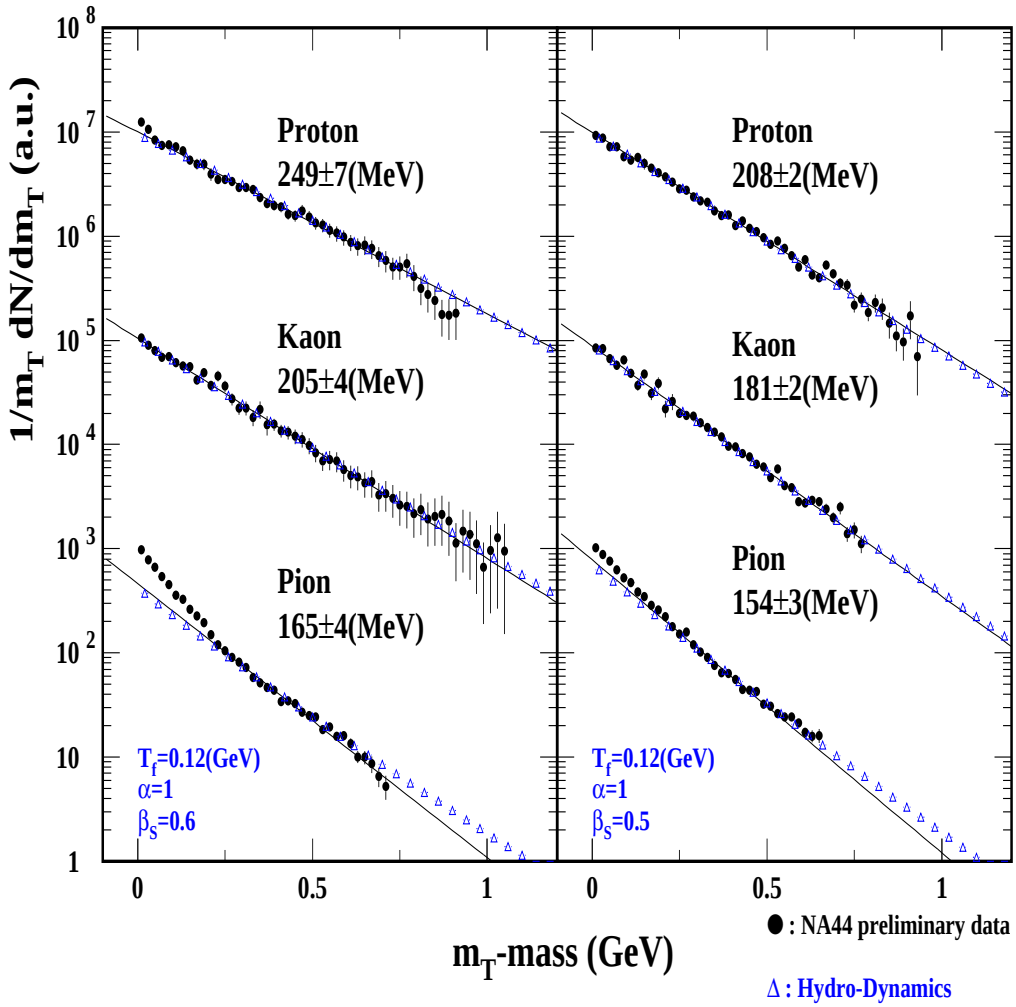

Figure 6-14: transverse mass spectra at T_f=120 MeV

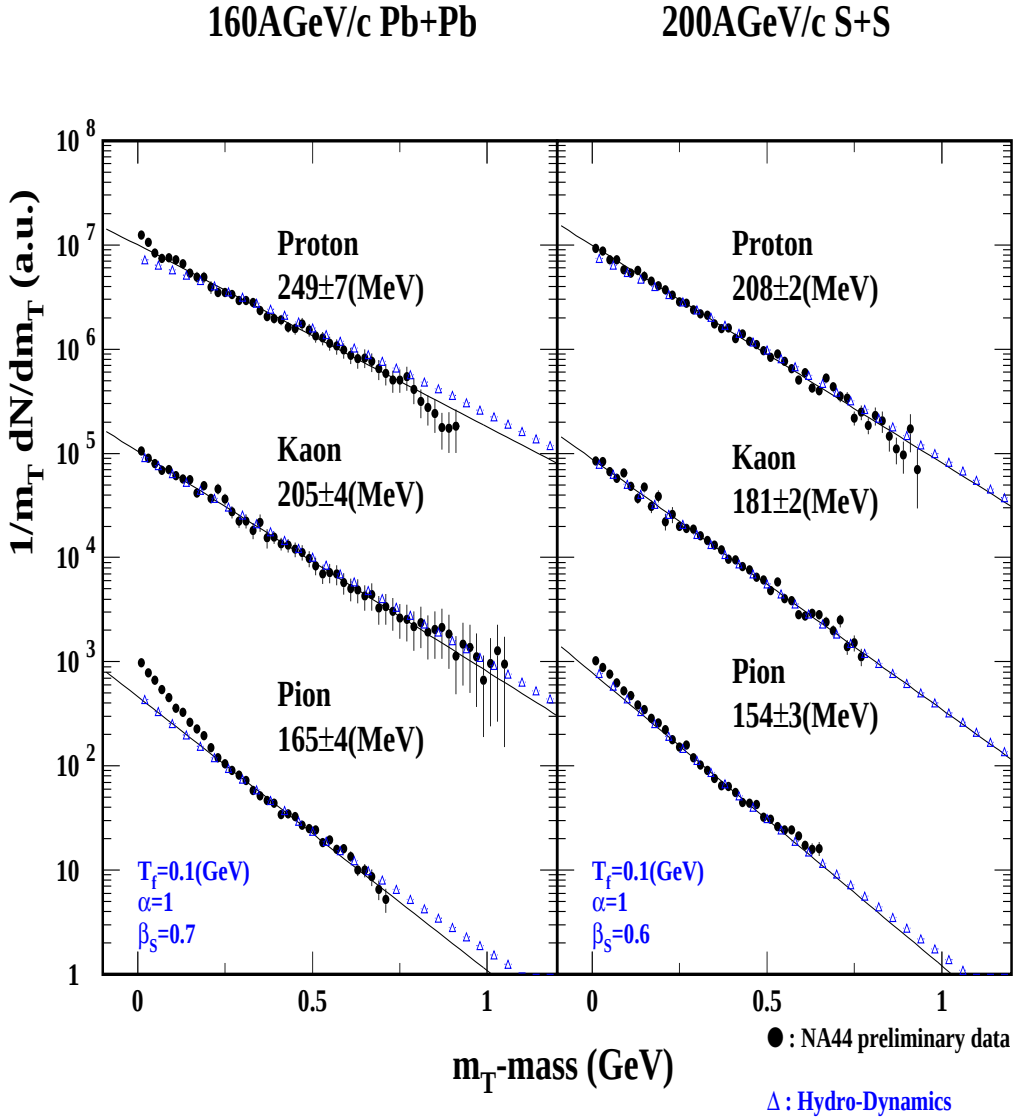

Figure 6-15: transverse mass spectra at T_f=100 MeV

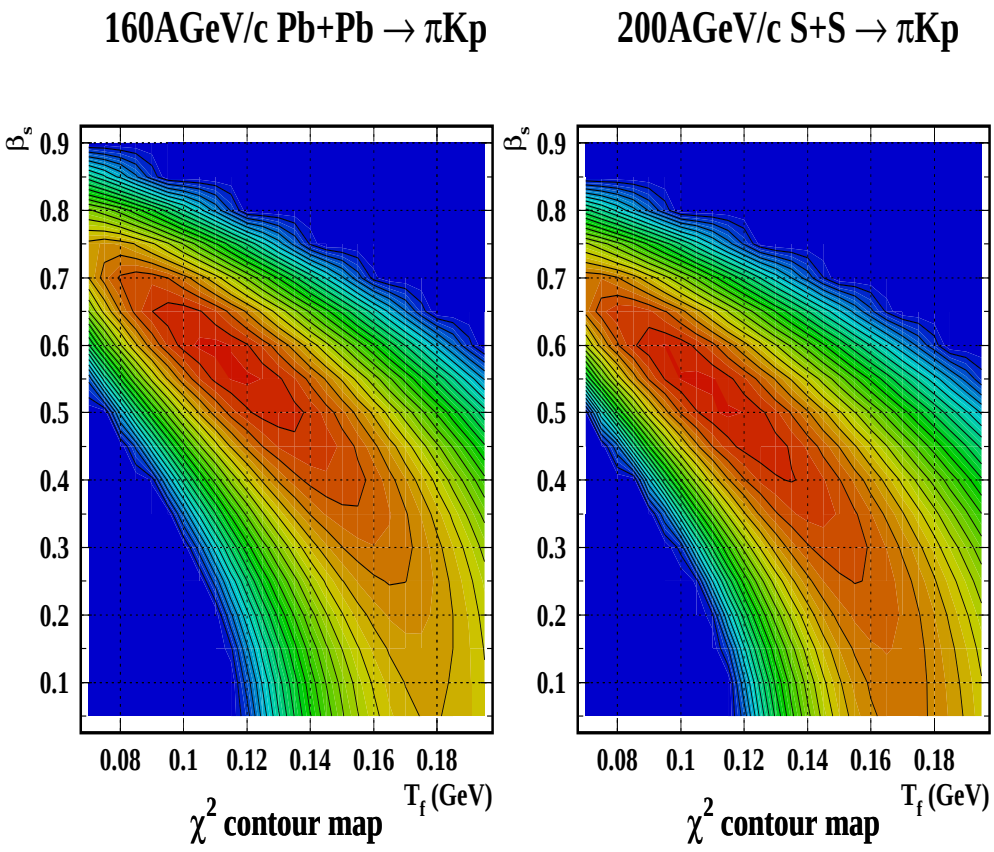

Figure 6-16: chi-square contour map over T_f and β_s

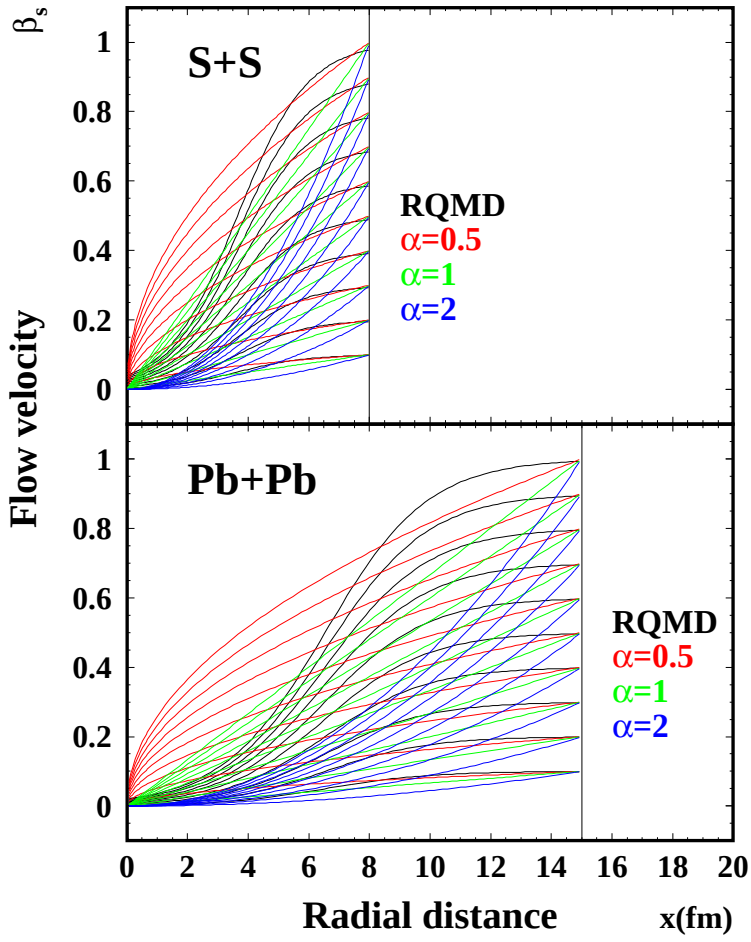

Figure 6-17: velocity profile

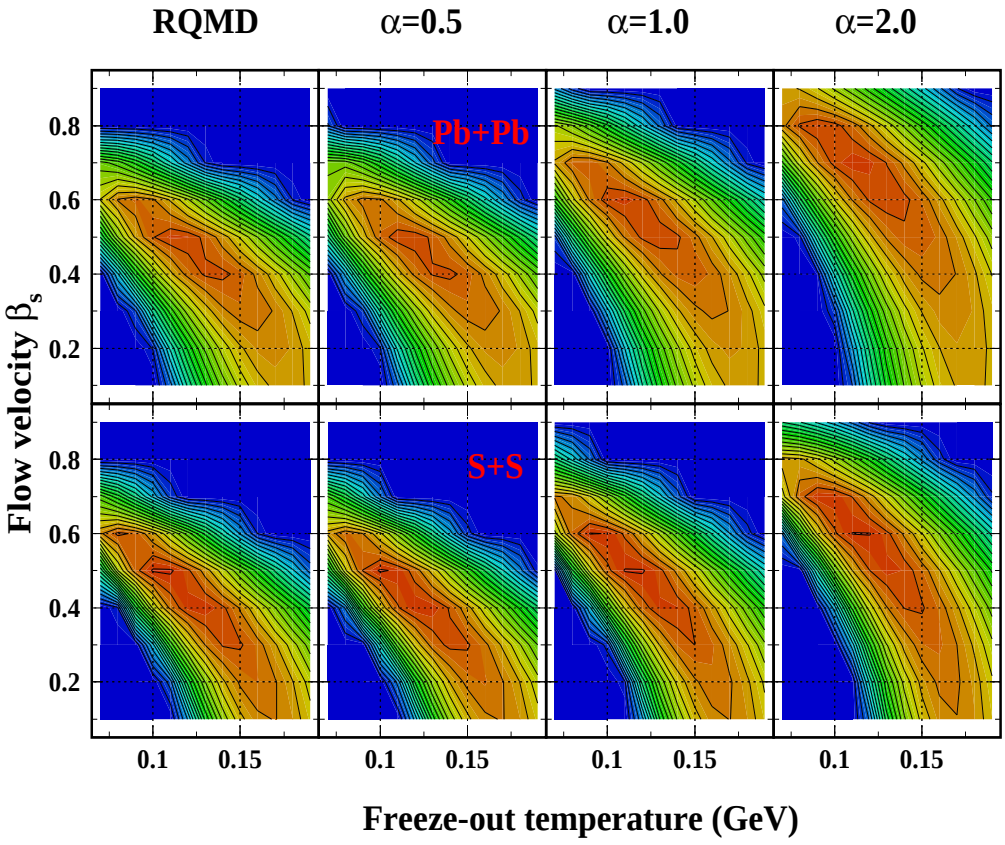

Figure 6-18: velocity profile dependence of chi-square map

Chapter 7. Conclusions

Proton rapidity distributions and transverse momentum spectra of hadrons at around the central rapidity have been measured for symmetric heavy-ion collisions S+S and Pb+Pb in NA44 at SPS. The nuclear stopping power was found to increase with the size of the colliding system by the amount of the observed stopped protons at mid-rapidity and the shape of the rapidity distributions of protons. We observed the systematic increase of the slope parameter with the particle mass and the colliding system, which had not seen in binary proton on proton collisions as seen from the summary plot of the fitted slope parameters. These phenomena are intuitively suggesting the hydro-dynamical transverse flow, which explains the measured slopes with one fixed freeze-out temperature and one fixed maximum flow velocity and the mass difference of the secondary particles for each colliding system. An increase between two colliding systems is explained by an increase of the flow velocity in this picture. We conclude that by using the symmetric collision from p+p, S+S to Pb+Pb, the existence of the higher degree of nuclear stopping power is proved at SPS energy and NA44 data are consistent with the following scenario that the high nuclear stopping power creates the large transverse flow in heavy ion collision and its increase with the colliding system.

Two particle interferometry measurements for pions and kaons with 200 AGeV/c S+Pb collisions are done around central rapidity. Measured transverse size of pion at high P_T region and that of kaon, where transverse momentum distributions are well explained by the same freeze-out conditions for all hadrons as mentioned above, are found to be similar and smaller than that of pion at low P_T region, where there is a large low P_T rise caused by the heavy resonances contribution. This is also consistent with the picture that the freeze-out happens at the same temperature and with the same transverse volume and the same transverse flow velocity for all hadrons, suggesting that a thermalization might be already achieved locally in the heavy-ion collisions and the locally thermalized fire ball is expanding collectively.

The cascade model RQMD reproduces the global trend of the M_T slopes and dN/dy for proton in the measured experimental data, although pion spectra at low P_T region deviates from the experimental measurement. This tells that the cascading process in the RQMD simulation makes the collective effect described by the hydro-dynamical model. This hydro-dynamical flow effect is found to increase with the size of the colliding system, because of the larger re-scatterings during the collisions caused by the higher baryon stopping at mid-rapidity in truly larger heavy-ion collisions.

Acknowledgements

The NA44 Collaboration thanks the staff of the CERN PS-SPS accelerator complex for their excellent work. We thank the technical staff at CERN and the collaborating institutes for their valuable contribution. We are also grateful for the support given by the Science Research Council of Denmark; the Japanese Society for the Promotion of Science, and the Ministry of Education, Science and Culture, Japan; the Science Research Council of Sweden; the US Department of Energy; and the National Science Foundation.

I would like to thank to Prof.M.Yonezawa and Prof.O.Miyamura for their helpful encouragements, to Prof.Y.Sumi, Prof.T.Sugitate and Dr.A.Sakaguchi for their continuous advices and discussions, to Dr.S.Nishimura for teaching me a lot about hodoscopes, to Prof.H.Boggild, Prof.C.W.Fabjan, Prof.T.Humanic, Prof.B.Jacak, Prof.B.Lorstad and Prof.W.Willis for their advices, to Dr.A.Franz for working with me in the experimental zone and counting house and for inviting me for party in his house, to Mr.K.Bussmann for his help on hardwares and spectrometer movement and for giving me several cups of coffee, to Mr.G.DiTore for his helping on electronics especially for DanPhysic high voltage, to Dr.G.Poulard for his managing the NA44 software, to Dr.F.Piuz and Prof.G.Paic for their skill to make TIC work, to Mr.N.Maeda for working with me on a lot of experimental works and living with me at St.Genis apartment and his skillful driving, to Dr.H.Kalechofsky for teaching me single particle analysis, to Dr.S.Pandey for teaching me two particle correlation and for inviting me to his wild party, to Mis.R.Jayanti for discussing with me a lot and for helping me to start up hodoscopes, to Dr.J.Dodd for climbing mountains with me, to Dr.J.Sullivan for teaching me RQMD and working with me on the tracking software and inviting me for dinner at his home several times, to Dr.H.van Hecke for teaching me database, to Dr.N.Xu for his helpful advices and for living and drinking and discussing with me about physics and life and oriental philosophy in the apartment at Los Alamos, to Dr.D.Fields for discussing with me several things, to Dr.J.Simon-Gillo for organizing analysis group, to Dr.M.Murray for his helpful discussions, to Dr.A.Miyabayashi for training me to do weight lifting, to Mr.A.Medvedev for helping me on the calibration and teaching me how to drink vodka, to Mr.M.Potekhin for discussions, to Mis.B.Holzer for teaching me how to climb a precipice, to Mr.M.Spegel for working with me on the tracking chamber software, to Mr.J.Sorensen for working with me on the TIC detector, to Mr.N.Matsumoto and Mr.H.Ohnishi and Mr.K.Kaimi for their help and discussions, to Mr.M.Kaneta for working with me on TIC software and for teaching me how to use scanner to make one on the figure in this thesis, to Mr.H.Shiota for working with me on TIC software and installing NA44 library into alpha osf and for proving us there is no difference between iteration and mapping if we do right, to all colleagues in hadron and high-intermediate energy laboratory for valuable and helpful discussions, to all my fiends who I have ever met for being as they are, to my parents and my sister and my grand mather and my relatives for their continuous support, and I would like to dedicate this thesis to my wife and coming our baby.

References

1-1 J.Schukraft, Nucl. Phys. **A553**, 31c(1993)

2-1 H.Boggild et al., Phys. Lett. **B349**, 386(1995)

2-2 H.Beker et al., Phys. Rev. Lett. **74**, 3340(1995)

2-3 H.Beker et al., Zeit. Phys. **C64**, 209(1994)

2-4 H.Boggild et al., Phys. Lett. **B302**, 510(1993)

2-5 T.Kobayashi and T.Sugitate, Nucl. Instr. and Meth. **A287**, 389(1990)

2-6 N.Maeda et al., Nucl. Instr. and Meth. **A346**, 132(1994)

5-1 E.V.Shuryak and O.V.Zhirov, Phys. Lett. **89B**, 253(1980)

5-2 J.Bachler et al., Phys. Rev. Lett. **72**, 1419(1994)

6-1 A.Jahns, C.Spieles, H.Sorge, H.Stocker and W.Greiner, Phys. Rev. Lett. **72**, 3465(1994)

6-2 E.Schnedermann, J.Sollfrank and U.Heinz, Phys. Rev. **C48**, 2462(1993)

6-3 P.B.Munzinger, J.Stachel, J.P.Wessels and N.Xu, Phys. Lett. **B344**, 43(1995)